Planck intermediate results. XXXIV. The magnetic field structure in the Rosette Nebula

N. Aghanim, M. I. R. Alves, M. Arnaud, D. Arzoumanian, J. Aumont, C. Baccigalupi, A. J. Banday, R. B. Barreiro, N. Bartolo, E. Battaner, et al.

To cite this version:

N. Aghanim, M. I. R. Alves, M. Arnaud, D. Arzoumanian, J. Aumont, et al.. Planck intermediate results. XXXIV. The magnetic field structure in the Rosette Nebula. Astronomy and Astrophysics - A&A, 2016, 586, pp.A137. 10.1051/0004-6361/201525616 . hal-03645222

HAL Id: hal-03645222
https://hal.science/hal-03645222v1

Submitted on 23 May 2022

A&A 586, A137 (2016)
DOI: 10.1051/0004-6361/201525616
© ESO 2016

Astronomy & Astrophysics

Planck intermediate results

XXXIV. The magnetic field structure in the Rosette Nebula

Planck Collaboration: N. Aghanim[55], M. I. R. Alves[55,87,9,⋆], M. Arnaud[67], D. Arzoumanian[55], J. Aumont[55], C. Baccigalupi[80], A. J. Banday[87,9], R. B. Barreiro[60], N. Bartolo[27,61], E. Battaner[88,89], K. Benabed[56,86], A. Benoit-Lévy[21,56,86], J.-P. Bernard[87,9], M. Bersanelli[30,45], P. Bielewicz[87,9,80], A. Bonaldi[63], L. Bonavera[60], J. R. Bond[8], J. Borrill[12,83], F. R. Bouchet[56,86], F. Boulanger[55], A. Bracco[55], C. Burigana[44,28,46], E. Calabrese[85], J.-F. Cardoso[68,1,56], A. Catalano[69,66], A. Chamballu[67,14,55], H. C. Chiang[24,7], P. R. Christensen[76,33], S. Colombi[56,86], L. P. L. Colombo[20,62], C. Combet[69], F. Couchot[65], B. P. Crill[62,77], A. Curto[6,60], F. Cuttaia[44], L. Danese[80], R. D. Davies[63], R. J. Davis[63], P. de Bernardis[29], A. de Rosa[44], G. de Zotti[41,80], J. Delabrouille[1], C. Dickinson[63], J. M. Diego[60], H. Dole[55,54], S. Donzelli[45], O. Doré[62,11], M. Douspis[55], A. Ducout[56,52], X. Dupac[35], G. Efstathiou[57], F. Elsner[21,56,86], T. A. Enßlin[72], H. K. Eriksen[58], E. Falgarone[66], K. Ferrière[87,9], F. Finelli[44,46], O. Forni[87,9], M. Frailis[43], A. A. Fraisse[24], E. Franceschi[44], A. Frejsel[76], S. Galeotta[43], S. Galli[56], K. Ganga[1], T. Ghosh[55], M. Giard[87,9], E. Gjerløw[58], J. González-Nuevo[60,80], K. M. Górski[62,90], A. Gregorio[31,43,49], A. Gruppuso[44], V. Guillet[55], F. K. Hansen[58], D. Hanson[74,62,8], D. L. Harrison[57,64], S. Henrot-Versillé[65], D. Herranz[60], S. R. Hildebrandt[62], E. Hivon[56,86], M. Hobson[6], W. A. Holmes[62], A. Hornstrup[15], W. Hovest[72], K. M. Huffenberger[22], G. Hurier[55], A. H. Jaffe[51], T. R. Jaffe[87,9], J. Jewell[62], M. Juvela[23], R. Keskitalo[12], T. S. Kisner[71], J. Knoche[72], M. Kunz[16,55,2], H. Kurki-Suonio[23,40], G. Lagache[5,55], J.-M. Lamarre[66], A. Lasenby[6,64], M. Lattanzi[28], C. R. Lawrence[62], R. Leonardi[35], F. Levrier[66], M. Liguori[27], P. B. Lilje[58], M. Linden-Vørnle[15], M. López-Caniego[60], P. M. Lubin[25], J. F. Macías-Pérez[69], B. Maffei[63], D. Maino[30,45], N. Mandolesi[44,4,28], A. Mangilli[56], M. Maris[43], P. G. Martin[8], E. Martínez-González[60], S. Masi[29], S. Matarrese[27,61,38], A. Melchiorri[29,47], L. Mendes[35], A. Mennella[30,45], M. Migliaccio[57,64], M.-A. Miville-Deschênes[55,8], A. Moneti[56], L. Montier[87,9], G. Morgante[44], D. Mortlock[52], A. Moss[82], D. Munshi[81], J. A. Murphy[75], P. Naselsky[76,33], F. Nati[29], P. Natoli[28,3,44], C. B. Netterfield[18], F. Noviello[63], D. Novikov[79], I. Novikov[76], N. Oppermann[8], L. Pagano[29,47], F. Pajot[55], R. Paladini[53], D. Paoletti[44,46], F. Pasian[43], G. Patanchon[1], O. Perdereau[65], V. Pettorino[39], F. Piacentini[29], M. Piat[1], D. Pietrobon[62], S. Plaszczynski[65], E. Pointecouteau[87,9], G. Polenta[3,42], N. Ponthieu[55,50,51], G. W. Pratt[67], G. Prézeau[11,62], S. Prunet[56,86], J.-L. Puget[55], R. Rebolo[59,13,34], M. Reinecke[72], M. Remazeilles[63,55,1], C. Renault[69], A. Renzi[32,48], I. Ristorcelli[87,9], G. Rocha[62,11], C. Rosset[1], M. Rossetti[30,45], G. Roudier[1,66,62], J. A. Rubiño-Martín[59,34], B. Rusholme[53], M. Sandri[44], D. Santos[69], M. Savelainen[23,40], G. Savini[78], D. Scott[19], J. D. Soler[55], L. D. Spencer[81], V. Stolyarov[6,64,84], D. Sutton[57,64], A.-S. Suur-Uski[23,40], J.-F. Sygnet[56], J. A. Tauber[36], L. Terenzi[37,44], L. Toffolatti[17,60,44], M. Tomasi[30,45], M. Tristram[65], M. Tucci[16], J. Tuovinen[10], L. Valenziano[44], J. Valiviita[23,40], B. Van Tent[70], P. Vielva[60], F. Villa[44], L. A. Wade[62], B. D. Wandelt[56,86,26], I. K. Wehus[62], H. Wiesemeyer[73], D. Yvon[14], A. Zacchei[43], and A. Zonca[25]

(Affiliations can be found after the references)

Received 5 January 2015 / Accepted 8 April 2015

ABSTRACT

Planck has mapped the polarized dust emission over the whole sky, making it possible to trace the Galactic magnetic field structure that pervades the interstellar medium (ISM). We combine polarization data from *Planck* with rotation measure (RM) observations towards a massive star-forming region, the Rosette Nebula in the Monoceros molecular cloud, to study its magnetic field structure and the impact of an expanding H II region on the morphology of the field. We derive an analytical solution for the magnetic field, assumed to evolve from an initially uniform configuration following the expansion of ionized gas and the formation of a shell of swept-up ISM. From the RM data we estimate a mean value of the line-of-sight component of the magnetic field of about 3 μG (towards the observer) in the Rosette Nebula, for a uniform electron density of about 12 cm^{-3}. The dust shell that surrounds the Rosette H II region is clearly observed in the *Planck* intensity map at 353 GHz, with a polarization signal significantly different from that of the local background when considered as a whole. The *Planck* observations constrain the plane-of-the-sky orientation of the magnetic field in the Rosette's parent molecular cloud to be mostly aligned with the large-scale field along the Galactic plane. The *Planck* data are compared with the analytical model, which predicts the mean polarization properties of a spherical and uniform dust shell for a given orientation of the field. This comparison leads to an upper limit of about 45° on the angle between the line of sight and the magnetic field in the Rosette complex, for an assumed intrinsic dust polarization fraction of 4%. This field direction can reproduce the RM values detected in the ionized region if the magnetic field strength in the Monoceros molecular cloud is in the range 6.5–9 μG. The present analytical model is able to reproduce the RM distribution across the ionized nebula, as well as the mean dust polarization properties of the swept-up shell, and can be directly applied to other similar objects.

Key words. ISM: magnetic fields – polarization – radiation mechanisms: general – radio continuum: ISM – submillimeter: ISM

[⋆] Corresponding author: M. I. R. Alves, e-mail: `marta.alves@irap.omp.eu`

1. Introduction

Stellar bubbles are formed from the combined action of ionization power and stellar winds from OB stars. They are a major source of turbulent energy injection into the interstellar medium (ISM), sweeping up the surrounding gas and dust and modifying the magnetic fields (e.g. Ferrière 2001). Bubbles are seen as agents of triggered star formation, as the swept-up material may become unstable and fragment. It is therefore important to understand the influence of star formation and feedback on the structure of the magnetic field, and how the ionized bubbles are shaped by the field. The all-sky polarization data from *Planck*[1] open up new opportunities for studying the magnetic field structure of such objects and their connection with the large-scale Galactic field.

The interplay between the expansion of an ionized nebula and the action of the magnetic fields has been the subject of several studies, both observational (e.g. Pavel & Clemens 2012; Santos et al. 2012, 2014) and numerical (e.g. Bernstein & Kulsrud 1965; Giuliani 1982; Ferrière et al. 1991; Krumholz et al. 2007; Peters et al. 2011; Arthur et al. 2011). These observational studies rely partly on interstellar dust grains as tracers of the magnetic field. Non-spherical grains spin around their axes of maximal inertia, which are precessing around the magnetic field lines. The grains emit preferentially along their long axes, thus giving rise to an electric vector perpendicular to the magnetic field. At the same time, dust grains polarize the light from background stars and since extinction is higher along their longest axes, the transmitted electric vector is parallel to the magnetic field in the plane of the sky (see e.g. Martin 2007). Observations of dust emission or absorption allow us to retrieve the plane-of-the-sky orientation of the magnetic field that pervades interstellar matter. Results from high-resolution studies of H II regions have revealed regions of well-ordered magnetic field along the edges of the nebulae and magnetic field strengths of tens to hundreds of μG. Santos et al. (2014) studied the star-forming region Sh2-29 in optical and near-infrared polarimetry and derived a field strength of around 400 μG. The authors used the Chandrasekhar-Fermi method (Chandrasekhar & Fermi 1953), which relates the dispersion in magnetic field orientation with turbulent motions of the gas, under the assumption of equipartition between magnetic and turbulent/thermal pressures. Such high values of the field strength reflect the ordered structure of the magnetic field at sub-parsec scales, compressed by the expanding H II region. The aforementioned dust polarization observations of ionized nebulae, both in emission and extinction, have covered small regions around the objects, generally tens of arcminutes. *Planck* data allow us to study the magnetic fields probed by polarized dust emission towards large H II regions embedded in their parent molecular clouds, and the diffuse medium surrounding them.

Measurements of the magnetic fields towards H II regions can also be performed through Faraday rotation of linearly polarized background sources, both extragalactic and Galactic (Heiles & Chu 1980). The plasma in the H II regions rotates the plane of polarization of the background radio wave by an angle that is proportional to the square of the observing wavelength. The quantity derived from Faraday rotation observations, the rotation measure (RM), is directly related to the line-of-sight component of the magnetic field $B_{\parallel}$ weighted by the electron density of the ionized gas. Harvey-Smith et al. (2011) studied the line-of-sight magnetic field towards five large diameter Galactic H II regions, tens of parsecs wide, using RM combined with Hα data to estimate the electron density. They found $B_{\parallel}$ values of 2–6 μG, consistent with those measured in the diffuse ISM through Zeeman splitting observations (Heiles & Crutcher 2005; Crutcher et al. 2010; Crutcher 2012). This indicates that the RM enhancement observed towards H II regions may be the consequence of a local increase of the electron density. A similar study performed on the Rosette Nebula by Savage et al. (2013) attributed the high values of RM to an increase in the field strength, as will be discussed in Sect. 2.

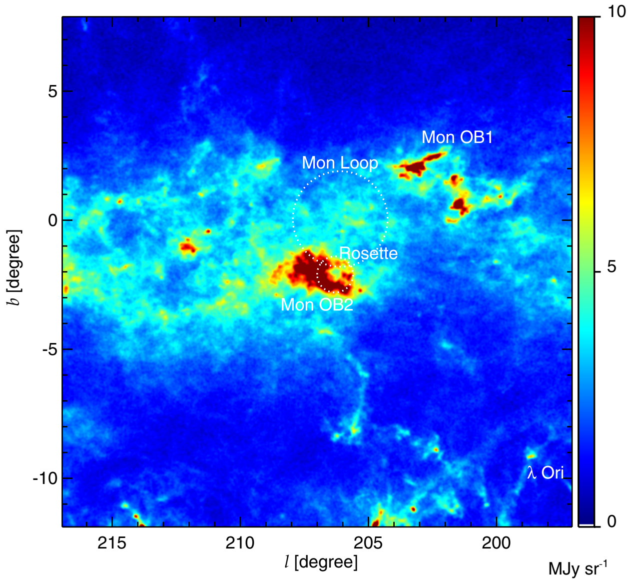

Fig. 1. The Rosette Nebula, its molecular cloud Mon OB2, and their surrounding medium as seen by *Planck* at 353 GHz. The dotted lines give the approximate outer radii of the Rosette H II region and the Mon Loop supernova remnant (described in Sect. 2). The northern Monoceros cloud Mon OB1 is above the Galactic plane; part of the dust ring of λ Ori is visible at the bottom right corner of the map; the northern end of Orion B is seen at $(l, b) = (204°, -12°)$ (Dame et al. 2001).

The goal of this work is to study the structure of the magnetic field in and around an ionized bubble created by young stars. For this purpose we chose the Rosette Nebula, adjacent to the Monoceros (Mon) OB2 cloud, for its close to spherical shape and for its relatively large size on the sky, $1\overset{\circ}{.}4$, relative to the *Planck* 353 GHz beam of $4\overset{\prime}{.}9$. This paper is organized as follows. We start in Sect. 2 by describing the Rosette Nebula and its main features relevant for our study. In Sect. 3 we introduce the *Planck* and ancillary data used in this study, which are then analysed and discussed in Sect. 4. The interpretation of the radio and submillimetre polarization observations is presented in Sect. 5, in light of a 2D analytical model of the magnetic field in a spherical bubble-shell structure. The main results are summarized in Sect. 6. The detailed derivation of our magnetic field model is given in Appendix A.

2. The Rosette Nebula and the Mon OB2 molecular cloud

The Rosette bubble is located near the anti-centre of the Galactic disk, centred on $(l, b) = (206\overset{\circ}{.}3, -2\overset{\circ}{.}1)$, and is part of a larger

---

[1] *Planck* (`http://www.esa.int/Planck`) is a project of the European Space Agency (ESA) with instruments provided by two scientific consortia funded by ESA member states (in particular the lead countries France and Italy), with contributions from NASA (USA) and telescope reflectors provided by a collaboration between ESA and a scientific consortium led and funded by Denmark.

region called the northern Monoceros region. It is at (1.6 ± 0.1) kpc from the Sun and its age is estimated to be about (3 ± 1) Myr (Román-Zúñiga & Lada 2008). Figure 1 shows the position of the Rosette Nebula relative to its parent molecular cloud Mon OB2, as well as other known and nearby objects, marked on the *Planck* 353 GHz map (Sect. 3.1). The Rosette has been the object of extensive studies, as it has been considered an archetype of a triggered star formation site (Williams et al. 1994; Balog et al. 2007; Román-Zúñiga & Lada 2008; Schneider et al. 2010). However, based on the small age spread among the young stellar objects in the Rosette, Ybarra et al. (2013) and Cambrésy et al. (2013) suggest that the effect of the H II region expansion on stimulating star formation is secondary relative to the original collapse of the cloud. The prominent OB association, NGC 2244, responsible for the ionized nebula and the evacuation of its central part, contains more than 100 stars, of which seven are O and 24 are B stars (Ogura & Ishida 1981; Marschall et al. 1982; Park & Sung 2002; Román-Zúñiga & Lada 2008). Cox et al. (1990) quote a luminosity of $22 \times 10^5\,L_\odot$ for the brightest four O stars and 13 B stars of the central cluster.

The first study of the expansion of the H II region in the Rosette was done by Minkowski (1949). The author also noted the existence of "elephant trunks" and dark globules, from the analysis of photographic data, in the north-western edge of the central cavity (Herbig 1974; Schneps et al. 1980; Carlqvist et al. 1998, 2002). Globules are also seen in the south-eastern region in the *Herschel* images of the Rosette (Schneider et al. 2010), where the ionized nebula is interacting with the molecular cloud. The Rosette H II region is an ionization bounded Strömgren sphere (Menon 1962) and expands at a velocity of $\lesssim 15\,\mathrm{km\,s^{-1}}$ (Smith 1973; Fountain et al. 1979; Meaburn 1968). The mean electron temperature in the nebula, derived by Quireza et al. (2006), is 8500 K.

The Rosette H II region has a projected optical extent of about 1.°4. Celnik (1985) estimated the size of the nebula by fitting several shell models to observations at 1.4 and 4.7 GHz. The mean radial profile of the radio emission was reproduced by a model of a spherical shell with inner and outer radii of 7 and 19 pc, respectively, and constant electron density of $13.5\,\mathrm{cm^{-3}}$ (these values have been scaled from the distance of 1.42 kpc used by Celnik to the adopted distance of 1.6 kpc). Celnik also found that the ionized shell shows a radial density gradient out to an outer radius of 28 pc, with a mean electron density of about $5.7\,\mathrm{cm^{-3}}$. This model leads to a total mass of ionized matter of $1.2 \times 10^4\,M_\odot$, similar to the value of $1.3 \times 10^4\,M_\odot$ obtained for the spherical shell of constant density. The total molecular mass derived from ^{12}CO emission is $1.6 \times 10^5\,M_\odot$ (Heyer et al. 2006), of which 54% lies inside the Rosette H II region.

The magnetic field in the Rosette Nebula has been recently studied by Savage et al. (2013) using RM observations of background galaxies. They fit the RM data with a simple stellar bubble model (Whiting et al. 2009) that consists of an inner low-density cavity of shocked stellar wind and a shell of shocked and photoionized ISM material. The authors assume that the ambient magnetic field $\boldsymbol{B}_0$ outside the bubble has a strength $B_0 = 4\,\mu$G and that the field component in the shock plane is amplified by a factor of 4, appropriate for strong adiabatic shocks. Then by fitting the RM data to their model, they find that the angle between $\boldsymbol{B}_0$ and the line of sight is $\theta_0 = 72°$. The results of Savage et al. (2013) will be further discussed in Sect. 5.2.

Part of the northern Monoceros region has also been studied in polarization at radio frequencies by Xiao & Zhu (2012). These authors focused on the supernova remnant (SNR) Monoceros Loop, G205.7+0.1, north-west of the Rosette Nebula. The SNR and H II region are thought to be interacting (Davies et al. 1978; Smith 1973; Jaffe et al. 1997; Fountain et al. 1979; Gosachinskii & Khersonskii 1982). The polarization data presented by Xiao & Zhu (2012) do not cover the interface region between the two objects and show that the magnetic field in the Rosette Nebula is largely parallel to the Galactic plane. However, at a frequency of 5 GHz the observed polarization vectors are the result of either highly rotated background polarized synchrotron emission, considering the high RMs of about $500\,\mathrm{rad\,m^{-2}}$ measured in the nebula (Sect. 4.2.2, Savage et al. 2013), or foreground emission.

3. Data

3.1. Planck data

Planck (Tauber et al. 2010; Planck Collaboration I 2011; Planck Collaboration I 2014) has mapped the polarization of the sky emission in seven frequency channels, from 30 to 353 GHz. In this paper we use the data from the High Frequency Instrument (HFI; Lamarre et al. 2010; Planck HFI Core Team 2011; Planck Collaboration VI 2014) at 353 GHz, where the dust polarized emission is brightest. A first description of the dust polarization sky is presented in a series of papers, namely Planck Collaboration Int. XIX (2015), Planck Collaboration Int. XX (2015), Planck Collaboration Int. XXI (2015), Planck Collaboration Int. XXX (2016), Planck Collaboration Int. XXXII (2016), and Planck Collaboration Int. XXXIII (2016).

3.1.1. Intensity and polarization

We use the full-mission temperature and polarization sky maps at 353 GHz from the 2015 release of *Planck* (Planck Collaboration I 2015). The map-making, calibration and correction of systematic effects is described in Planck Collaboration VIII (2015). We smooth the maps and their corresponding covariance from the initial angular resolution of 4.′9 to 6′. This is a compromise between increasing the signal-to-noise ratio of the polarization data and preserving high resolution, as well as minimizing beam depolarization effects.

The 353 GHz intensity data are corrected for the cosmic microwave background (CMB) anisotropies using the `Commander` map, presented in Planck Collaboration IX (2015), although the contribution to the total signal in the region under study is small, at most 2%. We also subtract the Galactic zero level offset, $0.0885 \pm 0.0067\,\mathrm{MJy\,sr^{-1}}$, from the intensity map and add the corresponding uncertainty to the intensity variance (Planck Collaboration VIII 2015). We do not attempt to correct for the polarized signal of the CMB anisotropies, as this is a negligible contribution $\ll 1\%$ at 353 GHz in the region under study (Planck Collaboration Int. XXX 2016).

The linear polarization of dust emission is measured from the Stokes parameters Q, U, and I, delivered in the *Planck* data release. They are the result of a line-of-sight integration and are related as

$$Q = Ip\cos(2\psi),$$

$$U = Ip\sin(2\psi),$$

$$p = \frac{P}{I} = \frac{\sqrt{Q^2 + U^2}}{I},$$

$$\psi = 0.5\arctan(U, Q), \tag{1}$$

where p is the dust polarization fraction and ψ is the polarization angle. The two argument function $\arctan(X, Y)$ is used to compute $\arctan(X/Y)$, avoiding the π ambiguity. The *Planck* Stokes parameters are provided in the `HEALPix` (Górski et al. 2005) convention, such that the angle $\psi = 0°$ is towards the north Galactic pole and positive towards the west (clockwise). In the commonly used IAU convention (Hamaker & Bregman 1996), the polarization angle is measured anticlockwise relative to the north Galactic pole. We adopt the IAU convention by taking the negative of the *Planck* U Stokes map.

The Stokes Q and U maps in the region under study have a typical signal-to-noise ratio of 8 and 2, respectively. The main systematic effect concerning polarization data is signal leakage from total intensity. We used the corrections derived from the global template fit, described in Planck Collaboration VIII (2015), which accounts for all of the leakage sources, namely bandpass, monopole, and calibration mismatches. The 2015 *Planck* data release also includes polarization maps that were corrected only for dust bandpass leakage using a different method. We compare the two sets of maps in the region under study to quantify the systematic uncertainties associated with the leakage correction. The relative difference in the Q Stokes parameter is less than 10%, whereas it is typically 25% in U because the Rosette is 2° from the Galactic plane, where the magnetic fields are largely parallel to the plane and contribute more signal to Q than to U.

Because of the presence of noise in the data, the polarization intensity, P, calculated directly using Eq. (1) is positively biased. We debias this quantity according to the method proposed by Plaszczynski et al. (2014) by taking into account the diagonal and off-diagonal terms in the covariance matrix for Q and U. Since we only calculate the polarization intensity towards high (>10) signal-to-noise regions, namely the Mon OB2 cloud, the relative difference between the debiased and direct (Eq. (1)) estimates is less than 3%. A comparison between other debiasing methods as applied to the all-sky *Planck* data is presented in Planck Collaboration Int. XIX (2015).

3.1.2. Products

We use the *Planck* "Type 3" CO map from Planck Collaboration XIII (2014) to qualitatively inspect the molecular gas in the Monoceros region. This is a composite line map, where the line ratios between the first three CO rotational lines are assumed to be constant across the whole sky. The Type 3 CO map is the highest signal-to-noise map extracted from *Planck*, with an angular resolution of 5′.5.

The dust emission from *Planck* wavelengths to about 100 μm is dominated by the contribution of large dust grains (radius larger than 0.05 μm). In order to trace their temperature, we use the map derived from the all-sky model of dust emission from Planck Collaboration XI (2014), at a resolution of 5′.

3.2. RM data

We use the RM data presented by Savage et al. (2013) towards 23 extragalactic radio sources observed through the Rosette complex with the Karl G. Jansky Very Large Array[2]. The RM observations towards extragalactic sources are an integral of the line-of-sight magnetic field component $B_{\parallel}$, weighted by the electron density n_e, and given by

$$\mathrm{RM} = 0.81 \int_0^S \left(\frac{n_e}{\mathrm{cm}^{-3}}\right)\left(\frac{B_{\parallel}}{\mu\mathrm{G}}\right)\left(\frac{\mathrm{d}s}{\mathrm{pc}}\right) \mathrm{rad\,m}^{-2}, \quad (2)$$

where S is the path length from the source to the observer. The RM is positive when $\boldsymbol{B}$ points towards us, hence when $B_{\parallel}$ is also positive.

We consider 20 measurements (given in Table 3 of Savage et al. 2013); two of the sources are depolarized and we also exclude the only negative RM value detected. This measurement was also discarded in the analysis of Savage et al. (2013), who could not determine if its origin is Galactic or extragalactic. In any case this measurement lies outside the boundaries of the Rosette Nebula. Whenever two values are given for the same source, in the case of a double component extragalactic object, we take their mean and the dispersion as the uncertainty because we combine the RM data at a resolution of 12′.8, with emission measure data at a lower resolution of 14′.4 (Sect. 3.3). The 20 RM measurements are positive and have a typical uncertainty of 40%, or below 10% for half of the sample.

3.3. Emission measure data

The emission measure (EM) data are from the radio recombination line (RRL) survey of Alves et al. (2015) at 1.4 GHz and at a resolution of 14′.4. These are a by-product of the H I Parkes All-Sky Survey (HIPASS, Staveley-Smith et al. 1996) and their analysis is presented by Alves et al. (2010, 2012). The emission measure is defined as

$$\mathrm{EM} = \int_0^{\infty} n_e^2 \mathrm{d}s \quad (3)$$

and derived from the integrated RRL emission as

$$\mathrm{EM} = 5.2 \times 10^{-4} \left(\frac{T_e}{\mathrm{K}}\right)^{1.5} \int \left(\frac{T_L \mathrm{d}\nu}{\mathrm{K\,kHz}}\right) \mathrm{cm}^{-6}\ \mathrm{pc}, \quad (4)$$

where T_e and T_L are the electron and line temperatures, respectively. The overall calibration uncertainty in these data is 10%.

3.4. IRAS data

We use the IRIS (Improved Reprocessing of the IRAS Survey, Miville-Deschênes & Lagache 2005) data at 12 and 100 μm. The IRAS map at 12 μm traces the emission from dust particles that are smaller than those emitting at the longer *Planck* wavelengths.

4. Our observational perspective on the Rosette

In this section we start by describing the features of the Rosette Nebula and its parent molecular cloud from total intensity maps at different frequencies. We then study the polarized emission arising from the dust shell that surrounds the Rosette H II region, along with the radio polarization signal created by the ionized gas.

4.1. Intensity

The Rosette Nebula and its parent molecular cloud are presented in Fig. 2. The maps show the RRL thermal radio emission, dust emission at 353 GHz, integrated CO emission, dust temperature,

---

[2] We checked for the presence of nearby pulsars in the Australia Telescope National Facility Pulsar Catalogue (Manchester et al. 2005). We did not find pulsars closer than 2° from the centre of the Rosette with the required information (distance, dispersion measure, RM).

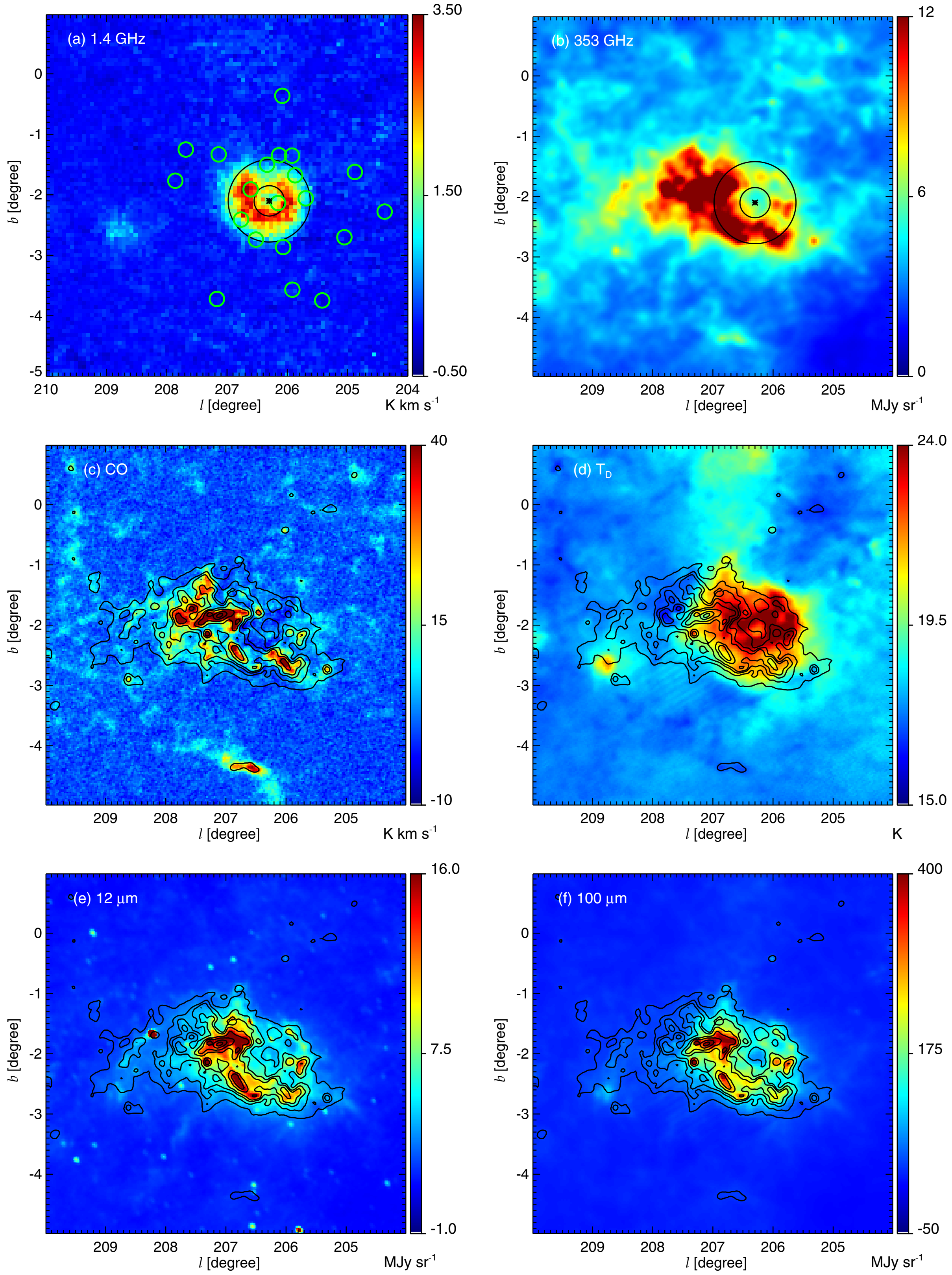

Fig. 2. The Rosette Nebula and its molecular cloud. **a)** Integrated RRL emission at $14\rlap{.}'4$ resolution, showing the radio morphology of the H II region. The green circles, with a diameter equivalent to the beam full width at half maximum (FWHM) of the RRL data, give the position of the 20 RM observations of Savage et al. (2013) used in this work. **b)** *Planck* 353 GHz emission at $6'$ resolution. The black star in panels **a)** and **b)** indicates the position of the central star cluster NGC 2244 and the black circles correspond to the inner and outer radii of the H II region, $r_{\rm in}^{\rm H\,II} = 7$ pc and $r_{\rm out}^{\rm H\,II} = 19$ pc, respectively (see Sect. 4.2.2). **c)** *Planck* CO integrated intensity at $5\rlap{.}'5$ resolution. **d)** Dust temperature derived from *Planck* at $5'$ resolution. **e)** Dust emission as seen by IRAS at $12\,\mu$m and at $100\,\mu$m (f), at $4'$ resolution. The contours in panels **c)** to **f)** show the *Planck* 353 GHz emission; these are at every 5% from 15 to 30%, at every 10% from 30 to 50%, and finally at 70 and 90% of the maximum intensity of 37 MJy sr^{-1}.

and dust emission at 12 μm and 100 μm. The central cavity is seen both in radio and in dust emission, as a lower intensity region around the position of the ionizing source NGC 2244.

The expanding H II region is interacting with the molecular cloud Mon OB2, creating photon-dominated regions at their interface (Cox et al. 1990; Schneider et al. 2010), which can be traced at 12 μm. The map of Fig. 2e shows bright 12 μm emission associated with the 353 GHz contours on the eastern side of the nebula's centre. Within these structures elongated along the ionization front, there are dense molecular clumps with on-going star formation, as the result of the compression by the H II region. The dust temperature is also higher at the interface of these regions with the nebula, as shown in Fig. 2d, compared to the lower temperature at the position of their maximum intensity.

Cox et al. (1990) studied the Rosette complex in all four IRAS bands and analysed the radial distribution of the dust emission. These authors showed that the 12 μm emission, which traces the photodissociation regions, comes from a shell surrounding the outer side of the ionization front, as well as from the molecular cloud. On the other hand, the longer wavelength emission at 60 and 100 μm mostly arises from the H II region and thus is tracing ionized and neutral gas.

The western part of the Rosette complex has not been studied as thoroughly as the main molecular cloud. It is not as bright in dust emission, but still visible in the *Planck* and IRAS maps (Figs. 2b, e, and f) as a fragmented shell surrounding the central cavity. There is no significant counterpart in CO emission, except in the cloud located in the south-west, which appears elongated perpendicular to the ionization front in the *Planck* and CO maps. This cloud also has lower dust temperature than the remainder of the western dust shell.

The dust shell seen in the *Planck* 353 GHz map surrounding the H II region is associated with the Rosette complex, as it correlates with the dust emission observed by IRAS (Cox et al. 1990) and identified in the dust temperature map. The map of Fig. 2d shows a clear enhancement of the dust temperature in the region occupied by the nebula as a result of dust heating by the central cluster. It also illustrates a decrease in the dust temperature towards the central cavity because the Rosette is not a filled H II region but a shell, with an inner cavity created by the evacuation of material due to powerful stellar winds (Smith 1973; Fountain et al. 1979).

The origin of the dust shell as material swept up by the expanding H II region will be further discussed in Sect. 5. The size of the shell can be estimated by fitting the *Planck* intensity map with a shell model, similar to that used by Celnik (1985) to derive the radius of the ionized nebula. We obtain $r_{\rm in}^{\rm dust} = 18$ pc and $r_{\rm out}^{\rm dust} = 22$ pc for the inner and outer radii of the dust shell, with a typical uncertainty of 2 pc. Further details are given in Appendix A.

4.2. Polarization

4.2.1. *Planck* data

The maps of the Q and U Stokes parameters towards the Rosette Nebula and its parent molecular cloud are shown in Figs. 3a and b, respectively. There is significant Q emission towards Mon OB2 relative to the background, however the polarized emission surrounding the Rosette H II region does not define the same shell as seen in intensity. Notably, the Q and U signal in some regions of the dust shell is at the same level as that outside the Rosette/Mon OB complex. Figure 4 compares the Q and U emission observed in the dust shell that surrounds the Rosette H II region (in red) with that from an aperture that represents the local background (in blue). The first distribution is measured within 22 pc (the outer radius of the dust shell, Sect. 4.1) from the central cluster and the second within an aperture of inner and outer radii of 2° and 3°, respectively, centred at $(l, b) = (207°, -2°)$ (see the circles in Fig. 3). As seen in Fig. 4a, the Q signal in the shell clearly deviates from that measured in the background, with a higher mean value and a broader distribution. The distribution of U emission, shown in Fig. 4b, is also broader in the dust shell, even if the mean level is similar to that of the background. We compare the histograms of Fig. 4 quantitatively by means of the Kolmogorov-Smirnov statistical test, which shows that the polarized signal from the shell and the background are significantly different. This test compares the cumulative distributions and thus takes into account the different number of points from each sample. The statistical difference applies when considering the dust shell as a whole, but it may not be valid in the case of individual structures located inside it. We will thus focus the analysis on the mean polarized quantities, without attempting to study the small-scale structure observed in the dust shell. This approach is also justified because our analytical magnetic field model is based on a uniform density distribution.

We estimate the mean value of the I, Q, and U Stokes parameters in the shell and background regions. These are listed in Table 1 along with the corresponding uncertainties, given by the standard error on the mean. The second to last column of Table 1 lists the mean of the Stokes parameters in the dust shell corrected for the background emission, required for comparison with the model results. We note that the choice of a constant value for the background follows from the absence of any clear pattern in the polarized emission outside the Rosette/Mon OB2 that we can use to model the background variations. As a result, the contribution of the background residuals to the polarized signal of the dust shell needs to be taken into account. The background distributions of Fig. 4 have about 8 times more points ($N_{\rm back} = 14\,154$) than those corresponding to the dust shell ($N_{\rm dust} = 1757$). We extract $N_{\rm dust}$ points from the background distribution and assess the variation of its mean Stokes parameters by repeating this exercise 10 000 times. We take the standard deviation of the 10 000 mean values and add it in quadrature to the standard error on the mean Stokes parameters. The final uncertainty in the background-subtracted values is quoted in the second to last column of Table 1. We also computed these quantities using a different leakage correction (as explained in Sect. 3.1.1), which we will use in Sect. 5.3 to quantify the systematic uncertainties in our results. We note that the method used to compute the uncertainties does not take into account that the background fluctuations are spatially correlated. If we estimate the background in circular areas of the same radius as the Rosette dust shell, we find a larger uncertainty on the background-corrected values. Thus, we cannot exclude that the mean Q and U values in Table 1 for the dust shell have a significant contribution from local background fluctuations. However, we regard the possibility of having a second ISM structure in the same direction as the Rosette as unlikely.

We perform the same analysis in the rectangular region of Fig. 3 that delineates the brightest part of Mon OB2. The mean Stokes parameters, corrected for the background contribution are listed in the last column of Table 1. We use these values to estimate the polarization properties of the Rosette's parent molecular cloud. The resulting debiased polarization fraction, derived according to the method introduced in Sect. 3.1.1, is $p = (3.8 \pm 0.9)\%$ and the polarization angle is $\psi = -3° \pm 14°$.

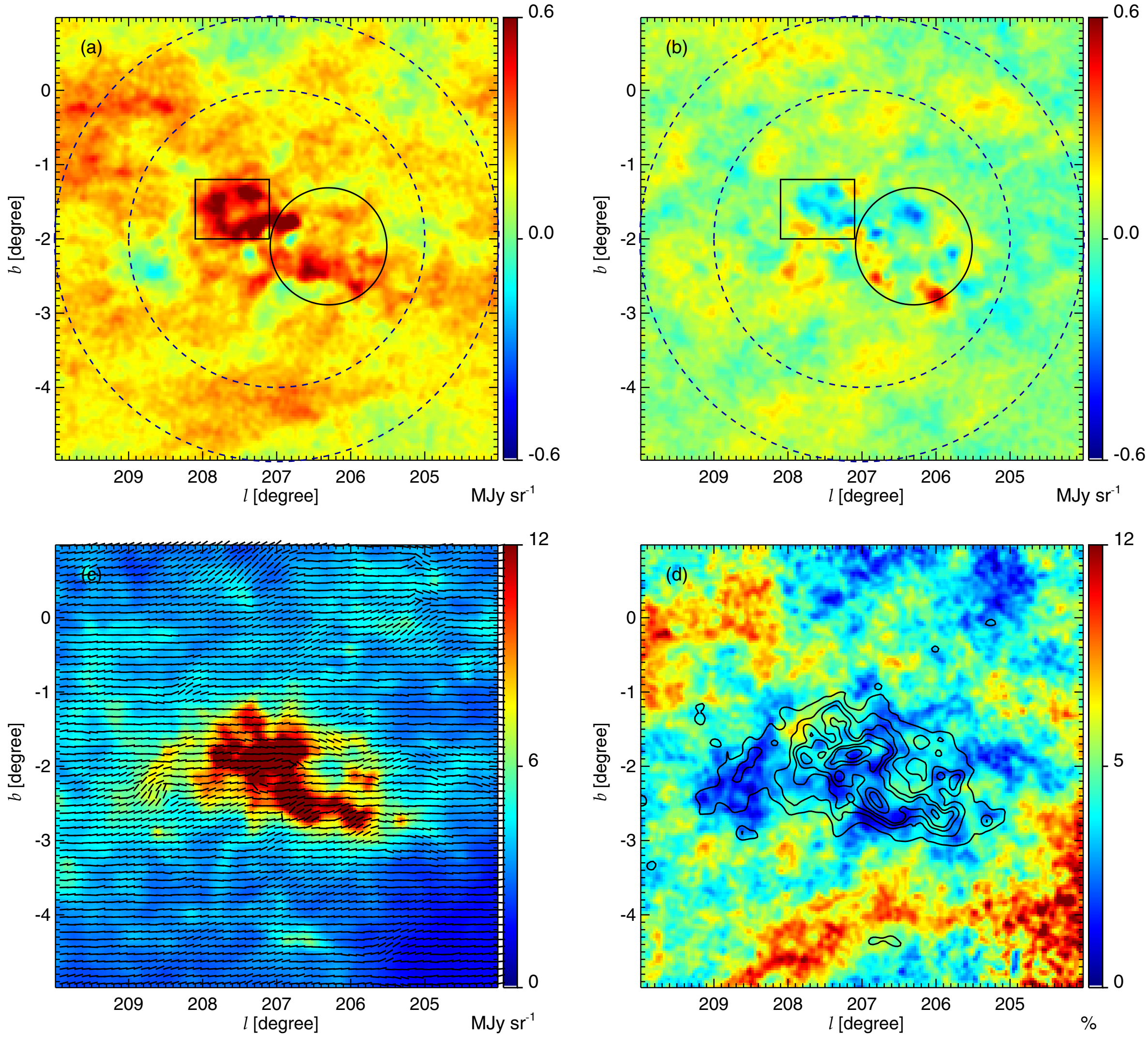

Fig. 3. *Planck* polarization maps of the Rosette region: **a)** Q Stokes parameter; **b)** U Stokes parameter. The dashed circles, with radii 2° and 3°, define the region where we estimate the background level, the full circle centred on the star cluster represents the outer radius of the dust shell, $r_{\rm out}^{\rm dust} = 22$ pc, and the rectangle encompasses the brightest part of the Mon OB2 cloud. **c)** Intensity map at 353 GHz with the plane-of-the-sky magnetic field orientation shown by headless vectors, obtained by rotating the polarization angle ψ by 90°. The vectors are plotted at every 6′, from the average of Q and U within the same distance from the central pixel. **d)** Polarization fraction p, with the same intensity contours as in Fig. 2.

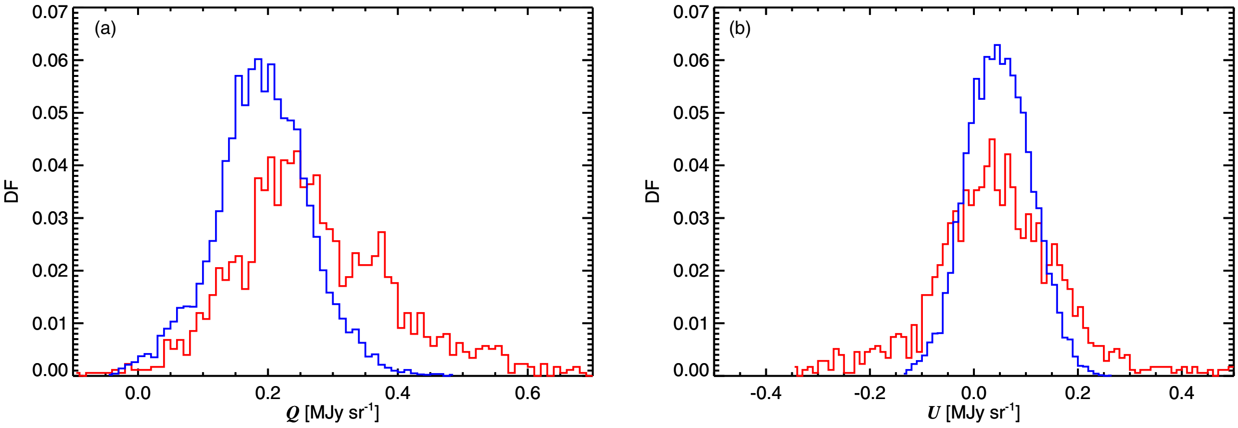

Fig. 4. Normalized distribution functions (DFs) of the **a)** Stokes Q and **b)** U maps measured within the background aperture (blue) and within the outer radius of the dust shell (red). The two regions are defined in Fig. 3 by the dashed and full circles, respectively.

Table 1. The mean level of the Stokes I, Q, and U parameters at 353 GHz, in units of MJy sr^{-1}.

Region	Dust shell	Mon OB2	Background	Difference: Shell	Difference: Mon OB2
$\langle I \rangle$	9.44 ± 0.08	10.6 ± 0.2	3.631 ± 0.006	5.80 ± 0.09	7.02 ± 0.2
$\langle Q \rangle$	0.278 ± 0.003	0.461 ± 0.005	0.1911 ± 0.0006	0.087 ± 0.004	0.270 ± 0.005
$\langle U \rangle$	0.045 ± 0.003	-0.004 ± 0.005	0.0488 ± 0.0005	-0.004 ± 0.004	-0.053 ± 0.005

Notes. The first three columns correspond to the dust shell, the Mon OB2 cloud and the background regions, respectively, as defined in the text and in Fig. 3. Their uncertainties are given by the standard error on the mean. The last two columns list the mean Stokes parameters in the dust shell and Mon OB2 cloud, respectively, corrected for the background contribution. The background subtraction is accounted for in the uncertainties as described in Sect. 4.2.1.

The plane-of-the-sky magnetic field orientation in Mon OB2, along the Galactic plane, is consistent with the large-scale orientation seen in Fig. 3c.

The map of polarization fraction is shown in Fig. 3d, where the lowest values of $p \lesssim 3\%$ are seen towards the densest regions surrounding the Rosette Nebula. Similar values are observed in the less bright part of the Mon OB2 cloud at $(l, b) = (208\overset{\circ}{.}5, -2\overset{\circ}{.}5)$. From the all-sky analysis of *Planck* 353 GHz polarization data, Planck Collaboration Int. XIX (2015) find that higher density regions have lower polarization fraction relative to the maximum $p_{\max} = 19.8\%$, detected at 1° resolution. This decrease in p can be the result of several effects, namely depolarization in the beam or along the line of sight, variations in the intrinsic polarization fraction of dust grains, as well as changes in the magnetic field geometry. The latter was shown to generally explain the variations of p across the whole sky: Planck Collaboration Int. XIX (2015) find an anti-correlation between the fluctuations in the magnetic field orientation and the polarization fraction. Planck Collaboration Int. XXXIII (2016) used this result to model the variations of the Stokes parameters across three interstellar filaments with variations of the magnetic field orientation, for a fixed alignment efficiency of dust grains. In Sect. 5 we present an analytical solution for the magnetic field in the Rosette H II region and associated dust shell, for constant dust properties. We will use this model to explain the present *Planck* polarization observations and the radio RM data consistently.

4.2.2. Radio data

The radio emission map of Fig. 2a shows the Rosette H II region and its nearly circular shape. We fit the radial profile of the RRL emission with a shell model and find the same values as Celnik (1985) for the inner and outer radii, $r_{\rm in}^{\rm H\,II} = 7$ pc and $r_{\rm out}^{\rm H\,II} = 19$ pc, respectively, with an uncertainty of 1 pc. Also shown in Fig. 2a are the positions of the RM data from Savage et al. (2013; Sect. 3.2). The circles have a diameter equivalent to the beam FWHM of the radio survey, $14\overset{\prime}{.}4$, in order to show the regions within which the electron density, $n_{\rm e}$, is estimated.

The RRL observations provide a measure of EM for a given electron temperature. We use Eq. (4) with $T_{\rm e} = 8500$ K (Sect. 2, Quireza et al. 2006) to calculate EM towards the 20 RM positions. The observed EM includes the contribution from the warm ionized gas from the background/foreground material in the Galaxy. We correct for this contribution by subtracting the average EM measured towards the RM positions located outside the H II region. Of the 20 positions, 14 lie outside the radius $r_{\rm out}^{\rm H\,II} = 19$ pc, with an average EM of $(288 \pm 124)\,{\rm cm}^{-6}$ pc, where the uncertainty corresponds to the standard error on the mean. The EM values measured towards the shell are in the range 1500–5300 cm^{-6} pc. We can thus estimate the electron density in the Rosette towards the remaining six positions, which are listed in Table 2. In the general case when the electron density distribution is not uniform but concentrated in discrete clumps of ionized gas, the filling factor f is introduced to relate the true path length L of a given line of sight through the nebula to the effective path length $L_{\rm eff} = fL$, which is the total length occupied by the individual clumps. The true path length through a shell of inner and outer radii $r_{\rm in}^{\rm H\,II}$ and $r_{\rm out}^{\rm H\,II}$, respectively, is given by (Savage et al. 2013)

Table 2. Results from the analysis of the RM and EM data.

Source	l [°]	b [°]	ξ [pc]	$\langle n_{\rm e} \rangle$ [cm^{-3}]	RM [rad m^{-2}]	$B_{\parallel}$ [μG]
I6	205.7	−2.1	17.0	9 ± 2	676 ± 68	5 ± 1
I7	206.2	−2.1	4.6	12 ± 1	594 ± 30	2.3 ± 0.2
I8	206.8	−2.4	16.0	12 ± 1	219 ± 113	1.1 ± 0.6
I10	205.9	−1.7	16.4	10 ± 1	709 ± 117	5 ± 1
I12	206.6	−1.9	9.6	13 ± 1	703 ± 26	2.1 ± 0.1
I15	206.3	−1.5	15.9	8 ± 1	501 ± 24	4 ± 1

Notes. Column 1 gives the RM source number, as in Savage et al. (2013); Cols. 2 and 3 list the Galactic coordinates of the source; Col. 4 gives the linear distance from the centre of the Rosette; Col. 5 lists the mean electron density estimated with Eq. (5) for $f = 1$; Col. 6 gives the RM data corrected for the background contribution; and the last column gives the line-of-sight component of the magnetic field estimated with Eq. (6) for $f = 1$. The uncertainties in both $\langle n_{\rm e} \rangle$ and $B_{\parallel}$ are statistical, and thus do not include the systematic uncertainties involved, namely those on the distance to the Rosette, its electron temperature, path length (which depends on the radii), electron density distribution, and the calibration uncertainty of the EM data.

$$L(\xi) = \begin{cases} 2r_{\rm out}^{\rm H\,II}\sqrt{1-\left(\xi/r_{\rm out}^{\rm H\,II}\right)^2} & \text{if } \xi \geq r_{\rm in}^{\rm H\,II} \\ 2r_{\rm out}^{\rm H\,II}\left[\sqrt{1-\left(\xi/r_{\rm out}^{\rm H\,II}\right)^2}\right. & \\ \left. - \left(r_{\rm in}^{\rm H\,II}/r_{\rm out}^{\rm H\,II}\right)\sqrt{1-\left(\xi/r_{\rm in}^{\rm H\,II}\right)^2}\right] & \text{if } \xi < r_{\rm in}^{\rm H\,II} \end{cases}$$

where ξ is the linear distance between a given line of sight and the line of sight to the centre of the nebula, measured in the transverse plane through the nebula. For the Rosette, with $r_{\rm in}^{\rm H\,II} = 7$ pc and $r_{\rm out}^{\rm H\,II} = 19$ pc as derived above, $L(\xi = 0) = 24$ pc is the path length through the centre of the shell.

The average electron density along the line of sight is estimated from the EM observations using Eq. (3) as

$$\langle n_{\rm e} \rangle = \sqrt{\frac{{\rm EM}f}{L}}. \tag{5}$$

Table 2 lists the average electron density at each of the six positions in the Rosette for $f = 1$. The derived values are between 8 and 13 $\mathrm{cm^{-3}}$ and are consistent with those obtained by Celnik (1985). The mean electron density across the entire H II region is 12.3 $\mathrm{cm^{-3}}$, with a scatter of 4 $\mathrm{cm^{-3}}$.

Similarly to the EM data, the measured values of RM include the contribution from the large-scale magnetic field weighted by the Galactic warm ionized gas. This needs to be corrected for in order to study the local component of the field in the Rosette. The mean of the 14 measurements outside the radius $r_{\mathrm{out}}^{\mathrm{H\,II}} = 19$ pc is (132 ± 20) rad $\mathrm{m^{-2}}$, where the uncertainty corresponds to the standard error on the mean. The background measurements vary between 50 and 230 rad $\mathrm{m^{-2}}$ (half of these have an uncertainty of more than 20%). The final six background-corrected RM values are listed in Table 2.

The line-of-sight component of the magnetic field can be obtained by combining the EM and RM observations, using Eqs. (2) and (3), as

$$B_{\parallel} = \frac{\mathrm{RM/rad\,m^{-2}}}{0.81\sqrt{(\mathrm{EM/cm^{-6}\,pc})(L/\mathrm{pc})f}}\,\mu\mathrm{G}. \qquad (6)$$

This approximation holds if $B_{\parallel}$ is uniform across the nebula and if n_{e} and $B_{\parallel}$ are uncorrelated along the line of sight. Beck et al. (2003) point out that the latter assumption can lead to uncertainties by a factor of 2–3 in the estimated value of $B_{\parallel}$. The derived $B_{\parallel}$ values in the nebula for $f = 1$ are listed in Table 2 and vary from +1 to +5 μG. If we consider a filling factor $f = 0.1$ (Herter et al. 1982; Kassim et al. 1989), the values increase by a factor of 3.2, varying between +3 and +16 μG. These results are in the range of the $B_{\parallel}$ values measured in the diffuse ISM (Crutcher 2012). As will be discussed in the next section, the hypothesis that the magnetic field is uniform throughout the Rosette H II region is not satisfied. The field is confined to the ionized shell and thus its direction must vary across the nebula. We will assess this aspect by means of a 2D magnetic field model and compare its predictions with the measured $B_{\parallel}$ values.

5. The magnetic field in the Rosette

In this section we interpret the observations by comparing them with the results from an analytical model of an ionized nebula that has expanded in a uniform and magnetized medium and formed a neutral shell of swept-up matter. The model is presented in Sect. 5.1 and further detailed in Appendix A. We use it to study the RM distribution across the nebula (Sect. 5.2), as well as to reproduce the mean polarization of the dust shell observed by *Planck* (Sect. 5.3).

5.1. The magnetized Strömgren shell

The evolution of an expanding ionized nebula has been studied numerically, both in uniform and turbulent magnetized media (e.g. Krumholz et al. 2007; Arthur et al. 2011). As the H II region expands, the surrounding ISM is swept up into a shell around the central stars. In accordance with the frozen-in condition, magnetic field lines are dragged with the expanding gas and concentrated in the dense shell. If the magnetic pressure is comparable to the thermal pressure in the H II region, magnetic forces lead to departures from sphericity. Furthermore, because the swept-up magnetic flux increases from the magnetic poles (along the direction of the initial field $\boldsymbol{B}_0$) to the equator (90° from $\boldsymbol{B}_0$), magnetic pressure in the swept-up shell tends to make the shell thickness similarly increase from the poles to the equator. We will ignore magnetic effects and assume that the H II region expands equally in all directions, creating a spherical neutral shell of swept-up ISM. We consider this assumption to be consistent with the radio observations of the Rosette H II region, which show its nearly circular shape (e.g. Fig. 2a), despite a possible elongation along the line of sight.

Within this framework, we derive an analytical solution for the magnetic field in a spherical structure composed of a shell of swept-up gas formed around a shell of ionized gas. This configuration is shown in Fig. A.1 of Appendix A, where the details of the derivation are discussed. The model is an analytical description of the correspondence between the initial and present configurations of the radial distribution of matter, which characterizes the expansion of the H II region. We consider that the initial gas density and the magnetic field $\boldsymbol{B}_0$ are uniform and that they evolve as the matter expands radially. This is translated in the form of an expansion law (Fig. A.2). The final magnetic field $\boldsymbol{B}$ (Eq. (A.8)) depends on the strength of the initial field, B_0, and its direction, described by the polar and azimuthal angles (θ_0, ϕ_0), with respect to the line of sight.

We note that the Galactic magnetic field has uniform and random components, which are of the same order (see e.g. Beck 2001). In the present study, $\boldsymbol{B}_0$ corresponds to the initial local field, which is a sample of the total (uniform plus random) magnetic field.

In the following sections we describe how the combination of RM and dust polarization data allows us to fully describe the magnetic field in the Rosette and its parent molecular cloud. These data have different resolutions; however, this is not a concern since the model does not attempt to reproduce any fluctuations on the scale of the resolution of either of the observables.

5.2. Ionized shell: RM

The RM of the modelled H II region is computed using Eq. (2). We consider a uniform nebula with constant electron density $n_{\mathrm{e}} = 12.3\,\mathrm{cm^{-3}}$, the mean value derived from the EM data (Sect. 4.2.2), and integrate $B_{\parallel}$ along the line-of-sight depth of the H II shell. Since the RM is derived solely from the line-of-sight component of the field, it does not depend on ϕ_0.

We derive the B_0 and θ_0 values that best fit the RM data through a χ^2-minimization procedure taking into account the corresponding uncertainties, as follows:

$$\chi^2 = \sum_{N_{\mathrm{points}}} \frac{(\mathrm{RM_{mod}} - \mathrm{RM_{obs}})^2}{\sigma^2_{\mathrm{RM,obs}}}. \qquad (7)$$

The reduced χ^2 is computed as $\chi^2_{\mathrm{r}} = \chi^2/N_{\mathrm{dof}}$, where $N_{\mathrm{dof}} = N_{\mathrm{points}} - N_{\mathrm{params}}$ is the number of degrees of freedom, the difference between the number of points and the number of parameters in the fit. In the present case $N_{\mathrm{params}} = 2$, corresponding to B_0 and θ_0. The results are shown in Fig. 5. Figure 5a presents the best-fit RM curve as a function of the linear distance to the centre of the nebula, ξ, along with the 20 RM measurements discussed in Sect. 4.2.2. The blue line is the result of a fit to the six RM data points within the outer radius of the Rosette Nebula, $\xi \le r_{\mathrm{out}}^{\mathrm{H\,II}} = 19$ pc, and hereafter referred to as the reference fit. The best-fit parameters are $B_0 = 7\,\mu$G and $\theta_0 = 25°$. The shape of the RM curve is set by the radii of the H II shell (thus by the expansion law used, Appendix A), and the scaling of the curve depends on a combination of the two free parameters. The model is unable to reproduce the scatter in the RMs observed close to the boundary of the H II region, which could be due to the possible clumpiness of the medium and/or fluctuations in the

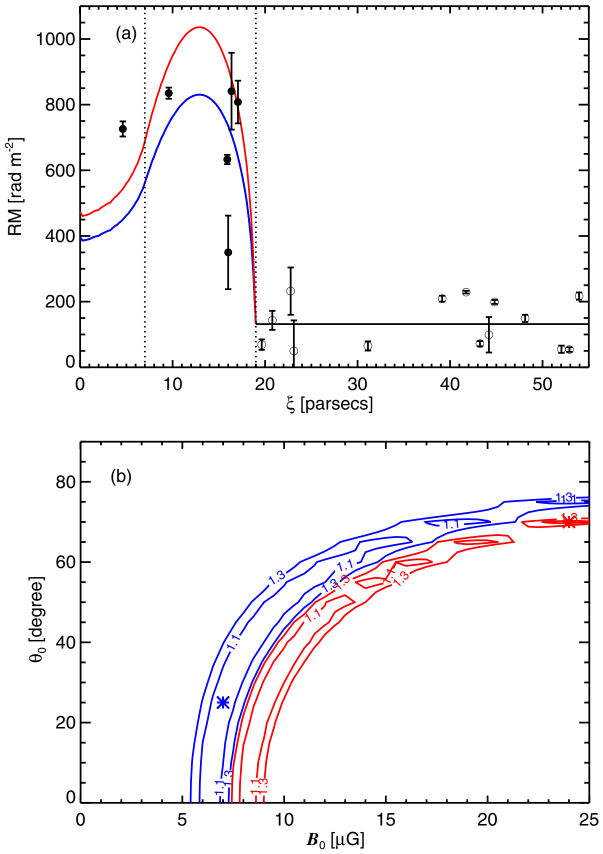

Fig. 5. Comparison between the RM observations and the predictions from the model. Panel **a)** shows the RM data as a function of the distance to the centre of the Rosette. The two vertical dashed lines show the inner and outer radii of the nebula, $r_{\rm in}^{\rm H\,II} = 7$ pc and $r_{\rm out}^{\rm H\,II} = 19$ pc, respectively (Sect. 4.2.2). The blue curve shows the radial profile of the modelled RM for the best fit to the six RM measurements within $r_{\rm out}^{\rm H\,II}$ (filled circles), the reference fit. The red curve is the result of fitting the highest four RM data points. The open circles correspond to the RM observations outside the Rosette, used to estimate the background RM, and are not included in the fit. Panel **b)** presents the reduced χ^2 from both fits. The stars indicate the best fit parameters B_0 and θ_0, which correspond to the minimum $\chi_{\rm r}^2$ for each fit. The reference fit (blue) gives $B_0 = 7\,\mu$G and $\theta_0 = 25°$ for $\chi^2 = 271$ and $N_{\rm dof} = 4$. The second fit (red) gives $B_0 = 24\,\mu$G and $\theta_0 = 70°$ for $\chi^2 = 76$ and $N_{\rm dof} = 2$. The contours are at 10 and 30% above the corresponding minimum values of $\chi_{\rm r}^2$.

magnetic field direction. These effects are not accounted for in our model, which also assumes that the expansion is perfectly spherical. We did not attempt to adjust the radii of the H II shell, or equivalently its expansion law. Instead, we perform a second fit, excluding the two lowest RM data points, at $\xi \sim 16$ pc, to assess the departures of the observations from the simplified assumptions of the present model. The result is shown by the red curve in Fig. 5a. The best-fit parameters are $B_0 = 24\,\mu$G and $\theta_0 = 70°$, for $\chi^2 = 76$ with $N_{\rm dof} = 2$, leading to a $\chi_{\rm r}^2$ that is about 30% lower than that obtained in the reference fit.

The χ^2 contours as a function of B_0 and θ_0 for the two fits are shown in Fig. 5b. The high χ^2 values (given in the caption) are due both to the simplicity of the model and to the uncertainties in the RM observations, which do not reflect their true radial variation across the Rosette, as they correspond to individual line-of-sight measurements. The contours illustrate the degeneracy between the strength and the orientation of the initial field relative to the line of sight, as expected since RM $\propto B_{\|} = B\cos\theta$ (Eq. (2)). As a consequence, all the (B_0, θ_0) combinations that

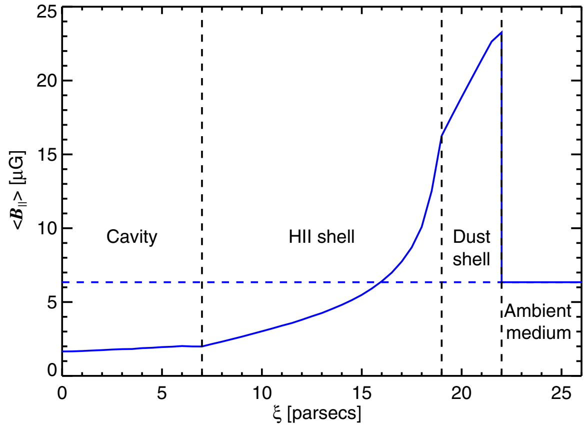

Fig. 6. Average of the line-of-sight component of the magnetic field as a function of the linear distance to the centre of the nebula. The curve shows the result of the reference fit, for which $B_0 = 7\,\mu$G, $\theta_0 = 25°$, and $B_{0\|} = 6.3\,\mu$G, as indicated by the horizontal dashed line. The three vertical lines delineate the inner and outer radii of the H II region and the outer radius of the dust shell: $r_{\rm in}^{\rm H\,II} = 7$ pc; $r_{\rm out}^{\rm H\,II} = 19$ pc; and $r_{\rm out}^{\rm dust} = 22$ pc.

follow the minimum $\chi_{\rm r}^2$ contour lead to approximately the same $B_{0\|}$ value: $B_{0\|} \simeq 6\,\mu$G for the reference fit and $B_{0\|} \simeq 8\,\mu$G for the second fit. Furthermore, for a given angle θ_0, the two different fits give B_0 values that differ by less than about $4\,\mu$G.

In the rest of this section, we consider only the reference fit obtained when using all of the six RM measurements (blue curve in Fig. 5). Figure 6 shows the radial profile of the mean of $B_{\|}$, $\langle B_{\|}\rangle$, measured along the line of sight. There is a significant difference between $\langle B_{\|}\rangle$ in the H II region and in the dust shell. We note that the exact shape of the curve is determined by the adopted expansion law (Fig. A.2), which characterizes the two distinct regimes in the evolution of the Rosette: the expansion of the ionized gas, leading to a decrease in B relative to B_0, and the compression of the interstellar gas in the dust shell, accompanied by a compression of the field lines, and hence an increase in B (see Fig. A.3). The mean value of $B_{\|}$ across the projected surface of the ionized shell, which in 3D includes the central cavity, is $2.6\,\mu$G. This is comparable to the mean of the six values derived from the RM data listed in Table 2. Therefore, the present model indicates that we can use the RM data to recover the mean $B_{\|}$ in the H II region, which is 62% lower than $B_{0\|}$ in the molecular cloud.

The RM observations are from Savage et al. (2013), who fitted a different analytical model to the data, as introduced in Sect. 2. The authors found a value of $\theta_0 = 72°$ for an assumed $B_0 = 4\,\mu$G, under the assumption that a strong adiabatic shock produces an enhancement of the component of the field parallel to the expansion front, relative to the ambient medium. In addition, Savage et al. (2013) applied the shock boundary conditions to the whole thickness of the shell, although these only hold in the thin-shell approximation. The present magnetic field solution in Eq. (A.8) naturally explains the variations of the normal and tangential components of the field relative to the expansion front, throughout the nebula.

This analysis defines the loci of B_0 and θ_0 values that best fit the RM data towards the Rosette Nebula (blue curve in Fig. 5b). For all of these solutions the resulting line-of-sight field component in the ambient medium is $B_{0\|} \simeq 6\,\mu$G, which is at the low end of the range of values reported by Crutcher (2012) for molecular clouds of similar column density as Mon OB2 (around 3×10^{22} cm^{-3}, Planck Collaboration XI 2014). In the following section we show that the degeneracy between B_0 and θ_0

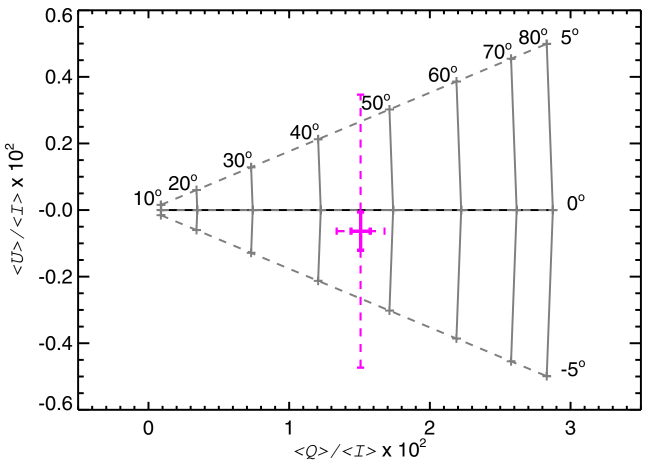

Fig. 7. Comparison between the *Planck* observations and the model. The ratios $\langle Q\rangle/\langle I\rangle$ and $\langle U\rangle/\langle I\rangle$ derived from the polarization data are given by the magenta point. The statistical and systematic uncertainties are shown by the solid and dashed error bars, respectively. The dashed grey lines show the solutions for $\phi_0 = -5°$, $0°$, and $5°$, with θ_0 varying from 10° to 80°. The solid grey lines indicate how the ratios change with ϕ_0, for a given θ_0 angle. The model results are calculated here for $p_0 = 4\%$.

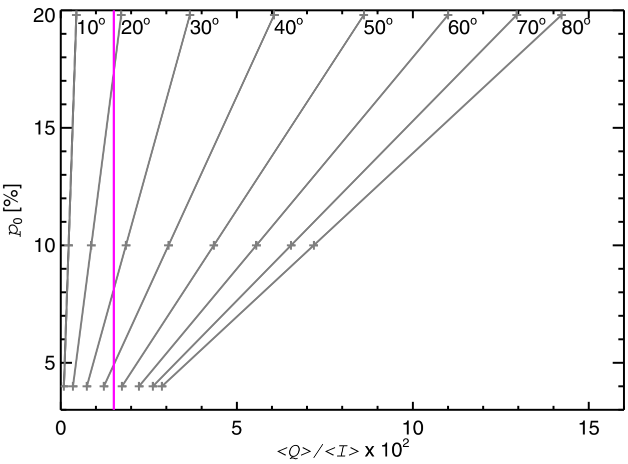

Fig. 8. Variation of the modelled $\langle Q\rangle/\langle I\rangle$ ratio as a function of p_0 and θ_0, for $\phi_0 = 0°$ (grey lines). The observed $\langle Q\rangle/\langle I\rangle$ ratio is shown by the vertical magenta line.

can be alleviated by further comparing the predictions from our model with the *Planck* polarization observations towards the dust shell.

5.3. Neutral shell: dust polarized emission

We model the shell that surrounds the H II region with constant intrinsic dust polarization fraction p_0 and with inner and outer radii of $r_{\rm in}^{\rm dust} = 19\,{\rm pc}$ and $r_{\rm out}^{\rm dust} = 22\,{\rm pc}$, respectively (see Appendix A). Since we will be comparing the ratios between the mean Stokes parameters, we do not specify the density or temperature of the gas and work with normalized quantities. The polarization fraction p can be written as $p = p_0 \sin^2\theta$. We compute $q = p_0 \sin^2\theta \cos(2\psi)$ and $u = p_0 \sin^2\theta \sin(2\psi)$ (Eq. (1)) at every position in the 3D shell and integrate along the line-of-sight direction to obtain the normalized Stokes parameter maps.

There are three variables involved in modelling the dust polarization: the angles (θ_0, ϕ_0), which define the direction of $\boldsymbol{B}_0$ with respect to the line of sight, and the intrinsic polarization fraction p_0. The Stokes parameters do not depend on the strength of the magnetic field. The polarization fraction relation given above indicates that p_0 and θ are degenerate. We thus start by comparing the data with the model for a fixed p_0 value of 4%, which corresponds to the observed value in the Mon OB2 cloud (Sect. 4.2.1). Figure 7 illustrates how the predicted ratios between the mean values of the Stokes parameters, $\langle Q\rangle/\langle I\rangle$ and $\langle U\rangle/\langle I\rangle$, vary as a function of the initial magnetic field direction (θ_0, ϕ_0). The observed ratios, calculated using the values listed in the fifth column of Table 1, are $\langle Q\rangle/\langle I\rangle = (1.51 \pm 0.07\,({\rm sta.}) \pm 0.17\,({\rm sys.})) \times 10^{-2}$ and $\langle U\rangle/\langle I\rangle = (-0.06 \pm 0.06\,({\rm sta.}) \pm 0.41\,({\rm sys.})) \times 10^{-2}$. The systematic uncertainties correspond to the difference in the ratios when derived with the different leakage correction maps (Sect. 3.1.1). The observed $\langle U\rangle/\langle I\rangle$ ratio constrains the sky projected orientation of the initial magnetic field, $\phi_0 \simeq 0°$, to within about 5°. This value is consistent with that measured towards the Rosette's parent molecular cloud (Sect. 4.2.1) and corresponds to a magnetic field parallel to the Galactic plane. Fixing this parameter allows us to study how the $\langle Q\rangle/\langle I\rangle$ ratio varies as a function of the angle between $\boldsymbol{B}_0$ and the line of sight θ_0, and the intrinsic polarization fraction p_0. This is shown in Fig. 8, for p_0 ranging from 4 to 19.8%, the maximum polarization fraction observed across the sky (Planck Collaboration Int. XIX 2015). The comparison between the data and the different models gives an upper limit on θ_0 of about 45° for $p_0 = 4\%$. A lower limit of $\theta_0 \simeq 20°$, implying a field that is nearly along the line of sight, is obtained for the maximum intrinsic polarization fraction $p_0 = 19.8\%$.

The comparison between the present model and the *Planck* polarization observations leads to two main results. First, the inferred range of θ_0, combined with the results from the RM study, restricts the range of the magnetic field strength in the Rosette's parent molecular cloud to $B_0 \simeq 6.5$–$9\,\mu$G. Second, we find that the Mon OB2 cloud has a magnetic field structure distinct from that of the Perseus spiral arm; an azimuthal Galactic mean field with a pitch angle of −8° (Ferrière 2011), is expected to be oriented at about 60° from the line of sight at the position of Mon OB2. Within the uniform density and polarization fraction assumption of this model, such values of θ_0 are only possible for a significantly low intrinsic polarization fraction p_0. However, we cannot discard depolarization effects from a turbulent field and/or clumpy density distribution. While several observational studies indicate that molecular clouds preserve the large-scale field orientation (see Li et al. 2014), *Planck* observations question this general interpretation of almost no variation of the magnetic fields with interstellar structures. Modelling of the dust polarization data from *Planck* allows us to study the 3D geometry of the magnetic field in a variety of environments. The analysis of the magnetic field structure in nearby interstellar filaments by Planck Collaboration Int. XXXIII (2016) suggests that their evolution is coupled to the field, which is distinct from the field of the clouds in which they are embedded. This result agrees with our findings on the Rosette/Mon OB2 complex.

Finally, we can estimate the magnetic and thermal pressures in the H II and dust shells. We do not include the possible contribution from a turbulent field at scales much smaller than the Rosette, whose quantification is difficult. In either case this is expected to be small owing to the fast expansion of the H II region, which tends to order the magnetic field. For an initial field strength $B_0 = 9\,\mu$G, which corresponds to $\theta_0 = 45°$, the modelled magnetic field has a mean value $B^{\rm H\,II} = 3.2\,\mu$G within the ionized nebula and $B^{\rm dust} = 21.4\,\mu$G in the dust shell. The thermal pressure in the H II region is $P_{\rm th}^{\rm H\,II} \simeq 2n_{\rm e}kT_{\rm e} = 2.9 \times 10^{-11}\,{\rm erg\,cm^{-3}}$, where k is the Boltzmann constant, $n_{\rm e} = 12.3\,{\rm cm^{-3}}$, and $T_{\rm e} = 8500\,{\rm K}$ (Sects. 2 and 4.2.2). The magnetic pressure, $P_{\rm mag}^{\rm H\,II} = (B^{\rm H\,II})^2/(8\pi) = 0.4 \times 10^{-12}\,{\rm erg\,cm^{-3}}$, is therefore smaller than the thermal pressure in the H II region, supporting our initial assumption that the H II region is roughly spherical. In the dust shell, the magnetic pressure is $P_{\rm mag}^{\rm dust} = 1.8 \times 10^{-11}\,{\rm erg\,cm^{-3}}$, hence smaller than but of the same order as the ionized gas pressure. This implies that both the thickness and the density of the dense shell should not be constant (e.g. Ferrière et al. 1991). Modelling these effects is beyond the simplified nature of the present analysis, where we focus on the mean polarization properties of the Rosette, but will be taken into account in future work.

6. Conclusions

This work represents the first joint analysis and modelling of radio and submillimetre polarization observations towards a massive star-forming region (the Rosette Nebula) to study its 3D magnetic field geometry. We have developed an analytical solution for the magnetic field, assumed to evolve from an initially uniform configuration following the expansion of ionized gas and the consequent concentration of the surrounding ISM in a dense shell. The assumption of uniform density and temperature distributions for both the ionized and dust shells, along with constant intrinsic polarization fraction of dust grains, is clearly an approximation. Different parts of the fragmented, swept-up shell presumably have distinct properties and some may even be pre-existing dense clouds caught by the expanding H II region. Nevertheless, the model is able to reproduce the mean observed quantities.

We use the *Planck* data at 353 GHz to trace the dust emission from the shell of swept-up ISM surrounding the Rosette H II region. Even if the shell is clearly seen in intensity, the same pattern is not detected in dust polarized emission against the local background. When analysed as a whole, the polarized signal from the dust shell is significantly distinct from that of the background and can be reproduced by the current model. The correspondence between the model and the *Planck* observations constrains the direction of the magnetic field in the Rosette's parent molecular cloud Mon OB2 to an angle in the plane of the sky $\phi_0 \simeq 0°$ (roughly parallel to the Galactic plane) and an angle to the line of sight $\theta \lesssim 45°$. This result is crucial to removing the degeneracy between θ_0 and B_0 inherent in the RM modelling. We thus find that B_0 is about 6.5–9 μG in Mon OB2.

The present magnetic field model provides a satisfactory fit to the observed RM distribution as a function of the distance from the centre of the Rosette H II region. More data are needed to better understand the abrupt variations of RM close to the outer radius of the nebula. The RM modelling suggests a significant increase in the line-of-sight magnetic field from the H II region to the dense shell, where $B_{\parallel}$ reaches nearly 4 times $B_{0\parallel}$.

The combination of RM and dust polarization data in this work is essential to constrain both the direction and the strength of the field in the Rosette region. The model presented here can be directly applied to other similar objects for which the expansion law can be derived.

Acknowledgements. We thank the referee for the useful comments. We acknowledge the use of the `HEALPix` package and IRAS data. The Planck Collaboration acknowledges the support of: ESA; CNES and CNRS/INSU-IN2P3-INP (France); ASI, CNR, and INAF (Italy); NASA and DoE (USA); STFC and UKSA (UK); CSIC, MICINN, and JA (Spain); Tekes, AoF, and CSC (Finland); DLR and MPG (Germany); CSA (Canada); DTU Space (Denmark); SER/SSO (Switzerland); RCN (Norway); SFI (Ireland); FCT/MCTES (Portugal); and DEISA (EU). A detailed description of the Planck Collaboration and a list of its members can be found at `http://www.rssd.esa.int/index.php?project=PLANCK&page=Planck_Collaboration`. The research leading to these results has received funding from the European Research Council under the European Union's Seventh Framework Programme (FP7/2007-2013)/ERC grant agreement No. 267934.

References

Alves, M. I. R., Davies, R. D., Dickinson, C., et al. 2010, MNRAS, 405, 1654
Alves, M. I. R., Davies, R. D., Dickinson, C., et al. 2012, MNRAS, 422, 2429
Alves, M. I. R., Calabretta, M., Davies, R. D., et al. 2015, MNRAS, 450, 2025
Arthur, S. J., Henney, W. J., Mellema, G., de Colle, F., & Vázquez-Semadeni, E. 2011, MNRAS, 414, 1747
Balog, Z., Muzerolle, J., Rieke, G. H., et al. 2007, ApJ, 660, 1532
Beck, R. 2001, Space Sci. Rev., 99, 243
Beck, R., Shukurov, A., Sokoloff, D., & Wielebinski, R. 2003, A&A, 411, 99
Bernstein, I. B., & Kulsrud, R. M. 1965, ApJ, 142, 479
Cambrésy, L., Marton, G., Feher, O., Tóth, L. V., & Schneider, N. 2013, A&A, 557, A29
Carlqvist, P., Kristen, H., & Gahm, G. F. 1998, A&A, 332, L5
Carlqvist, P., Gahm, G. F., & Kristen, H. 2002, Ap&SS, 280, 405
Celnik, W. E. 1985, A&A, 144, 171
Chandrasekhar, S., & Fermi, E. 1953, ApJ, 118, 113
Cox, P., Deharveng, L., & Leene, A. 1990, A&A, 230, 181
Crutcher, R. M. 2012, ARA&A, 50, 29
Crutcher, R. M., Wandelt, B., Heiles, C., Falgarone, E., & Troland, T. H. 2010, ApJ, 725, 466
Dame, T. M., Hartmann, D., & Thaddeus, P. 2001, ApJ, 547, 792
Davies, R. D., Elliott, K. H., Goudis, C., Meaburn, J., & Tebbutt, N. J. 1978, A&AS, 31, 271
Ferrière, K. 2011, Mem. Soc. Astron. It., 82, 824
Ferrière, K. M. 2001, Rev. Mod. Phys., 73, 1031
Ferrière, K. M., Mac Low, M.-M., & Zweibel, E. G. 1991, ApJ, 375, 239
Fountain, W. F., Gary, G. A., & Odell, C. R. 1979, ApJ, 229, 971
Giuliani, Jr., J. L. 1982, ApJ, 256, 624
Górski, K. M., Hivon, E., Banday, A. J., et al. 2005, ApJ, 622, 759
Gosachinskii, I. V., & Khersonskii, V. K. 1982, Sov. Astron., 26, 146
Hamaker, J. P., & Bregman, J. D. 1996, A&AS, 117, 161
Harvey-Smith, L., Madsen, G. J., & Gaensler, B. M. 2011, ApJ, 736, 83
Heiles, C., & Chu, Y.-H. 1980, ApJ, 235, L105
Heiles, C., & Crutcher, R. 2005, in Cosmic Magnetic Fields, eds. R. Wielebinski, & R. Beck (Berlin: Springer Verlag), Lect. Notes Phys., 664, 137
Herbig, G. H. 1974, PASP, 86, 604
Herter, T., Briotta, Jr., D. A., Gull, G. E., Shure, M. A., & Houck, J. R. 1982, ApJ, 262, 164
Heyer, M. H., Williams, J. P., & Brunt, C. M. 2006, ApJ, 643, 956
Jaffe, T. R., Bhattacharya, D., Dixon, D. D., & Zych, A. D. 1997, ApJ, 484, L129
Kassim, N. E., Weiler, K. W., Erickson, W. C., & Wilson, T. L. 1989, ApJ, 338, 152
Krumholz, M. R., Stone, J. M., & Gardiner, T. A. 2007, ApJ, 671, 518
Lamarre, J., Puget, J., Ade, P. A. R., et al. 2010, A&A, 520, A9
Li, H.-B., Goodman, A., Sridharan, T. K., et al. 2014, Protostars and Planets VI, 101
Manchester, R. N., Hobbs, G. B., Teoh, A., & Hobbs, M. 2005, AJ, 129, 1993
Marschall, L. A., van Altena, W. F., & Chiu, L.-T. G. 1982, AJ, 87, 1497
Martin, P. G. 2007, in EAS Pub. Ser. 23, eds. M.-A. Miville-Deschênes, & F. Boulanger, 165
Meaburn, J. 1968, Ap&SS, 1, 278
Menon, T. K. 1962, ApJ, 135, 394
Minkowski, R. 1949, PASP, 61, 151
Miville-Deschênes, M., & Lagache, G. 2005, ApJS, 157, 302
Ogura, K., & Ishida, K. 1981, PASJ, 33, 149
Park, B.-G., & Sung, H. 2002, AJ, 123, 892
Parker, E. N. 1970, ApJ, 162, 665
Pavel, M. D., & Clemens, D. P. 2012, ApJ, 760, 150
Peters, T., Banerjee, R., Klessen, R. S., & Mac Low, M.-M. 2011, ApJ, 729, 72
Planck HFI Core Team 2011, A&A, 536, A4
Planck Collaboration I. 2011, A&A, 536, A1
Planck Collaboration I. 2014, A&A, 571, A1
Planck Collaboration VI. 2014, A&A, 571, A6
Planck Collaboration XI. 2014, A&A, 571, A11
Planck Collaboration XIII. 2014, A&A, 571, A13
Planck Collaboration I. 2015, A&A, submitted [`arXiv:1502.01582`]
Planck Collaboration VIII. 2015, A&A, submitted [`arXiv:1502.01587`]
Planck Collaboration IX. 2015, A&A, submitted [`arXiv:1502.05956`]

Planck Collaboration Int. XIX. 2015, A&A, 576, A104
Planck Collaboration Int. XX. 2015, A&A, 576, A105
Planck Collaboration Int. XXI. 2015, A&A, 576, A106
Planck Collaboration Int. XXX. 2016, A&A, 586, A133
Planck Collaboration Int. XXXII. 2016, A&A, 586, A135
Planck Collaboration Int. XXXIII. 2016, A&A, 586, A136
Plaszczynski, S., Montier, L., Levrier, F., & Tristram, M. 2014, MNRAS, 439, 4048
Quireza, C., Rood, R. T., Bania, T. M., Balser, D. S., & Maciel, W. J. 2006, ApJ, 653, 1226
Román-Zúñiga, C. G., & Lada, E. A. 2008, Star Formation in the Rosette Complex, ed. B. Reipurth, 928
Santos, F. P., Roman-Lopes, A., & Franco, G. A. P. 2012, ApJ, 751, 138
Santos, F. P., Franco, G. A. P., Roman-Lopes, A., Reis, W., & Román-Zúñiga, C. G. 2014, ApJ, 783, 1
Savage, A. H., Spangler, S. R., & Fischer, P. D. 2013, ApJ, 765, 42
Schneider, N., Motte, F., Bontemps, S., et al. 2010, A&A, 518, L83
Schneps, M. H., Ho, P. T. P., & Barrett, A. H. 1980, ApJ, 240, 84
Smith, M. G. 1973, ApJ, 182, 111
Staveley-Smith, L., Wilson, W. E., Bird, T. S., et al. 1996, PASA, 13, 243
Tauber, J. A., Mandolesi, N., Puget, J., et al. 2010, A&A, 520, A1
Whiting, C. A., Spangler, S. R., Ingleby, L. D., & Haffner, L. M. 2009, ApJ, 694, 1452
Williams, J. P., de Geus, E. J., & Blitz, L. 1994, ApJ, 428, 693
Xiao, L., & Zhu, M. 2012, A&A, 545, A86
Ybarra, J. E., Lada, E. A., Román-Zúñiga, C. G., et al. 2013, ApJ, 769, 140

---

[1] APC, AstroParticule et Cosmologie, Université Paris Diderot, CNRS/IN2P3, CEA/lrfu, Observatoire de Paris, Sorbonne Paris Cité, 10 rue Alice Domon et Léonie Duquet, 75205 Paris Cedex 13, France
[2] African Institute for Mathematical Sciences, 6–8 Melrose Road, Muizenberg, 7950 Cape Town, South Africa
[3] Agenzia Spaziale Italiana Science Data Center, via del Politecnico snc, 00133 Roma, Italy
[4] Agenzia Spaziale Italiana, Viale Liegi 26, 00133 Roma, Italy
[5] Aix-Marseille Université, CNRS, LAM (Laboratoire d'Astrophysique de Marseille) UMR 7326, 13388 Marseille, France
[6] Astrophysics Group, Cavendish Laboratory, University of Cambridge, J J Thomson Avenue, Cambridge CB3 0HE, UK
[7] Astrophysics & Cosmology Research Unit, School of Mathematics, Statistics & Computer Science, University of KwaZulu-Natal, Westville Campus, Private Bag X54001, 4000 Durban, South Africa
[8] CITA, University of Toronto, 60 St. George St., Toronto, ON M5S 3H8, Canada
[9] CNRS, IRAP, 9 Av. colonel Roche, BP 44346, 31028 Toulouse Cedex 4, France
[10] CRANN, Trinity College, Pearse Street, Dublin 2, Ireland
[11] California Institute of Technology, Pasadena, CA 91125, California, USA
[12] Computational Cosmology Center, Lawrence Berkeley National Laboratory, Berkeley, CA 94720, California, USA
[13] Consejo Superior de Investigaciones Científicas (CSIC), Madrid, Spain
[14] DSM/Irfu/SPP, CEA-Saclay, 91191 Gif-sur-Yvette Cedex, France
[15] DTU Space, National Space Institute, Technical University of Denmark, Elektrovej 327, 2800 Kgs. Lyngby, Denmark
[16] Département de Physique Théorique, Université de Genève, 24 quai E. Ansermet, 1211 Genève 4, Switzerland
[17] Departamento de Física, Universidad de Oviedo, Avda. Calvo Sotelo s/n, 33007 Oviedo, Spain
[18] Department of Astronomy and Astrophysics, University of Toronto, 50 Saint George Street, Toronto, ON M5S 3H4, Canada
[19] Department of Physics & Astronomy, University of British Columbia, 6224 Agricultural Road, Vancouver, BC V6T 1Z4, British Columbia, Canada
[20] Department of Physics and Astronomy, Dana and David Dornsife College of Letter, Arts and Sciences, University of Southern California, Los Angeles, CA 90089, USA
[21] Department of Physics and Astronomy, University College London, London WC1E 6BT, UK
[22] Department of Physics, Florida State University, Keen Physics Building, 77 Chieftan Way, Tallahassee, FL 32306 Florida, USA
[23] Department of Physics, Gustaf Hällströmin katu 2a, University of Helsinki, 00100 Helsinki, Finland
[24] Department of Physics, Princeton University, Princeton, 1746, Elizabeth New Jersey, USA
[25] Department of Physics, University of California, Santa Barbara, CA 93106 California, USA
[26] Department of Physics, University of Illinois at Urbana-Champaign, 1110 West Green Street, Urbana, Illinois, USA
[27] Dipartimento di Fisica e Astronomia G. Galilei, Università degli Studi di Padova, via Marzolo 8, 35131 Padova, Italy
[28] Dipartimento di Fisica e Scienze della Terra, Università di Ferrara, via Saragat 1, 44122 Ferrara, Italy
[29] Dipartimento di Fisica, Università La Sapienza, P. le A. Moro 2, 00133 Roma, Italy
[30] Dipartimento di Fisica, Università degli Studi di Milano, via Celoria, 16 Milano, Italy
[31] Dipartimento di Fisica, Università degli Studi di Trieste, via A. Valerio 2, 34128 Trieste, Italy
[32] Dipartimento di Matematica, Università di Roma Tor Vergata, via della Ricerca Scientifica, 1, 00133 Roma, Italy
[33] Discovery Center, Niels Bohr Institute, Blegdamsvej 17, 2100 Copenhagen, Denmark
[34] Dpto. Astrofísica, Universidad de La Laguna (ULL), 38206 La Laguna, Tenerife, Spain
[35] European Space Agency, ESAC, Planck Science Office, Camino bajo del Castillo, s/n, Urbanización Villafranca del Castillo, 28692 Villanueva de la Cañada, Madrid, Spain
[36] European Space Agency, ESTEC, Keplerlaan 1, 2201 AZ Noordwijk, The Netherlands
[37] Facoltà di Ingegneria, Università degli Studi e-Campus, via Isimbardi 10, 22060 Novedrate (CO), Italy
[38] Gran Sasso Science Institute, INFN, viale F. Crispi 7, 67100 L'Aquila, Italy
[39] HGSFP and University of Heidelberg, Theoretical Physics Department, Philosophenweg 16, 69120 Heidelberg, Germany
[40] Helsinki Institute of Physics, Gustaf Hällströmin katu 2, University of Helsinki, 00100 Helsinki, Finland
[41] INAF–Osservatorio Astronomico di Padova, Vicolo dell'Osservatorio 5, 35141 Padova, Italy
[42] INAF–Osservatorio Astronomico di Roma, via di Frascati 33, Monte Porzio Catone, 00136 Roma, Italy
[43] INAF–Osservatorio Astronomico di Trieste, via G.B. Tiepolo 11, 34131 Trieste, Italy
[44] INAF/IASF Bologna, via Gobetti 101, 40127 Bologna, Italy
[45] INAF/IASF Milano, via E. Bassini 15, 20133 Milano, Italy
[46] INFN, Sezione di Bologna, via Irnerio 46, 40126 Bologna, Italy
[47] INFN, Sezione di Roma 1, Università di Roma Sapienza, Piazzale Aldo Moro 2, 00185 Roma, Italy
[48] INFN, Sezione di Roma 2, Università di Roma Tor Vergata, via della Ricerca Scientifica, 1, Roma, Italy
[49] INFN/National Institute for Nuclear Physics, via Valerio 2, 34127 Trieste, Italy
[50] IPAG: Institut de Planétologie et d'Astrophysique de Grenoble, Université Grenoble Alpes, IPAG, 38000 Grenoble, France
[51] CNRS, IPAG, 38000 Grenoble, France
[52] Imperial College London, Astrophysics group, Blackett Laboratory, Prince Consort Road, London, SW7 2AZ, UK
[53] Infrared Processing and Analysis Center, California Institute of Technology, Pasadena, CA 91125, USA
[54] Institut Universitaire de France, 103 bd Saint-Michel, 75005 Paris, France
[55] Institut d'Astrophysique Spatiale, CNRS (UMR 8617) Université Paris-Sud 11, Bâtiment 121, 91405 Orsay, France
[56] Institut d'Astrophysique de Paris, CNRS (UMR 7095), 98bis boulevard Arago, 75014 Paris, France

[57] Institute of Astronomy, University of Cambridge, Madingley Road, Cambridge CB3 0HA, UK
[58] Institute of Theoretical Astrophysics, University of Oslo, Blindern, 0371 Oslo, Norway
[59] Instituto de Astrofísica de Canarias, C/Vía Láctea s/n, La Laguna, 38205 Tenerife, Spain
[60] Instituto de Física de Cantabria (CSIC-Universidad de Cantabria), Avda. de los Castros s/n, Santander, Spain
[61] Istituto Nazionale di Fisica Nucleare, Sezione di Padova, via Marzolo 8, 35131 Padova, Italy
[62] Jet Propulsion Laboratory, California Institute of Technology, 4800 Oak Grove Drive, Pasadena, California, USA
[63] Jodrell Bank Centre for Astrophysics, Alan Turing Building, School of Physics and Astronomy, The University of Manchester, Oxford Road, Manchester, M13 9PL, UK
[64] Kavli Institute for Cosmology Cambridge, Madingley Road, Cambridge, CB3 0HA, UK
[65] LAL, Université Paris-Sud, CNRS/IN2P3, 91400 Orsay, France
[66] LERMA, CNRS, Observatoire de Paris, 61 avenue de l'Observatoire, 57014 Paris, France
[67] Laboratoire AIM, IRFU/Service d'Astrophysique – CEA/DSM – CNRS – Université Paris Diderot, Bât. 709, CEA-Saclay, 91191 Gif-sur-Yvette Cedex, France
[68] Laboratoire Traitement et Communication de l'Information, CNRS (UMR 5141) and Télécom ParisTech, 46 rue Barrault, 75634 Paris Cedex 13, France
[69] Laboratoire de Physique Subatomique et de Cosmologie, Université Joseph Fourier Grenoble I, CNRS/IN2P3, Institut National Polytechnique de Grenoble, 53 rue des Martyrs, 38026 Grenoble Cedex, France
[70] Laboratoire de Physique Théorique, Université Paris-Sud 11 & CNRS, Bâtiment 210, 91405 Orsay, France
[71] Lawrence Berkeley National Laboratory, Berkeley, 94720 California, USA
[72] Max-Planck-Institut für Astrophysik, Karl-Schwarzschild-Str. 1, 85741 Garching, Germany
[73] Max-Planck-Institut für Radioastronomie, Auf dem Hügel 69, 53121 Bonn, Germany
[74] McGill Physics, Ernest Rutherford Physics Building, McGill University, 3600 rue University, Montréal, QC, H3A 2T8, Canada
[75] National University of Ireland, Department of Experimental Physics, Maynooth, Co. Kildare, Ireland
[76] Niels Bohr Institute, Blegdamsvej 17, Copenhagen, Denmark
[77] Observational Cosmology, Mail Stop 367-17, California Institute of Technology, Pasadena, CA, 91125, USA
[78] Optical Science Laboratory, University College London, Gower Street, London, UK
[79] P.N. Lebedev Physical Institute of the Russian Academy of Sciences, Astro Space Centre, 84/32 Profsoyuznaya st., 117997 Moscow, GSP-7, Russia
[80] SISSA, Astrophysics Sector, via Bonomea 265, 34136 Trieste, Italy
[81] School of Physics and Astronomy, Cardiff University, Queens Buildings, The Parade, Cardiff, CF24 3AA, UK
[82] School of Physics and Astronomy, University of Nottingham, Nottingham NG7 2RD, UK
[83] Space Sciences Laboratory, University of California, Berkeley, California, USA
[84] Special Astrophysical Observatory, Russian Academy of Sciences, Nizhnij Arkhyz, Zelenchukskiy region, 369167 Karachai-Cherkessian Republic, Russia
[85] Sub-Department of Astrophysics, University of Oxford, Keble Road, Oxford OX1 3RH, UK
[86] UPMC Univ Paris 06, UMR 7095, 98bis boulevard Arago, 75014 Paris, France
[87] Université de Toulouse, UPS-OMP, IRAP, 31028 Toulouse Cedex 4, France
[88] University of Granada, Departamento de Física Teórica y del Cosmos, Facultad de Ciencias, 18071 Granada, Spain
[89] University of Granada, Instituto Carlos I de Física Teórica y Computacional, 18071 Granada, Spain
[90] Warsaw University Observatory, Aleje Ujazdowskie 4, 00-478 Warszawa, Poland

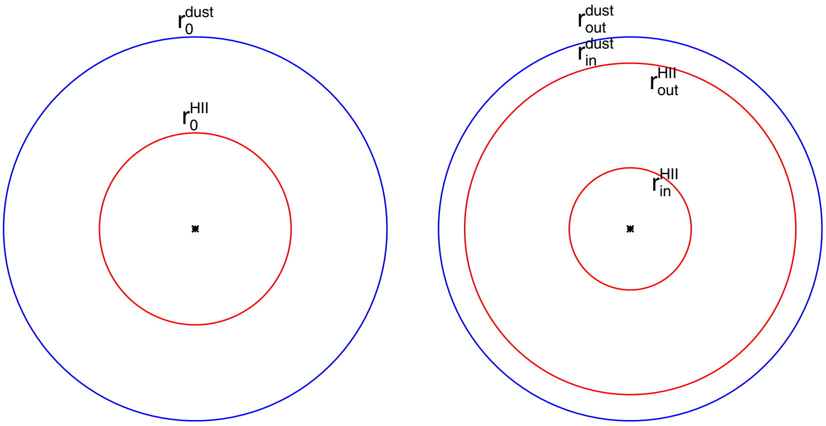

Fig. A.1. Sketch of the adopted spherical configuration. *Left*: the initial state, with uniform density and magnetic field; there are no separate ionized and dust shells. *Right*: present-day state with a cavity inside $r_{\rm in}^{\rm H\,II}$, an ionized shell between $r_{\rm in}^{\rm H\,II}$ and $r_{\rm out}^{\rm H\,II}$, and a dust shell between $r_{\rm in}^{\rm dust} = r_{\rm out}^{\rm H\,II}$ and $r_{\rm out}^{\rm dust}$. The present-day radii $r_{\rm in}^{\rm H\,II}$, $r_{\rm out}^{\rm H\,II}$, and $r_{\rm out}^{\rm dust}$ correspond to initial radii 0, $r_0^{\rm H\,II}$, and $r_0^{\rm dust}$, respectively.

Appendix A: Magnetic field model

In this appendix we present the derivation of the analytical formula that describes the magnetic field structure in a spherical shell, following the expansion of an ionized nebula in a uniform medium with density n_0 and magnetic field $\boldsymbol{B}_0$.

We start by deriving the expansion law, which will define how the initial uniform magnetic field is modified. Once the star cluster is formed, it ionizes the surrounding gas, which becomes overpressured and starts expanding at a velocity close to the ionized gas sound speed. The expansion of the ionized gas, in turn, creates a cavity and sweeps up the surrounding ISM into a thin and dense shell. The resulting structure, as observed at the present time, is composed of a cavity of radius $r_{\rm in}^{\rm H\,II}$, surrounded by a thick shell of ionized gas extending from $r_{\rm in}^{\rm H\,II}$ to $r_{\rm out}^{\rm H\,II}$, itself surrounded by a thin dust shell extending from $r_{\rm in}^{\rm dust}$ to $r_{\rm out}^{\rm dust}$ (see Fig. A.1). For the Rosette, $r_{\rm in}^{\rm H\,II} = 7$ pc and $r_{\rm out}^{\rm H\,II} = 19$ pc, as derived from the radial distribution of the radio emission (Sect. 4.2.2); $r_{\rm in}^{\rm dust} = 18$ pc and $r_{\rm out}^{\rm dust} = 22$ pc, measured from the *Planck* 353 GHz latitude cut through the centre of the shell (Sect. 4.1). Thus, the inner radius of the dust shell is slightly smaller than the outer radius of the H II region. This is not surprising, as the Rosette is an ionization bounded Strömgren sphere and thus the two shells are expected to overlap at the boundary, where the ionized and neutral gases are mixed. However, for the sake of simplicity, we take $r_{\rm in}^{\rm dust} = r_{\rm out}^{\rm H\,II} = 19$ pc.

We use a parameter grid of 1 pc resolution for all the radii. Therefore, we adopt an uncertainty of 1 pc in $r_{\rm in}^{\rm H\,II}$ and $r_{\rm out}^{\rm H\,II}$. We ascribe a larger uncertainty of 2 pc to $r_{\rm in}^{\rm dust}$ and $r_{\rm out}^{\rm dust}$; this reflects the variation of the fitted radii when considering the longitude or radial profile of the dust emission, which are affected by the presence of the Mon OB2 cloud.

We now denote by r_0 the initial radius of a particle currently at radius r. In our simplified model, the initial radius of a particle currently at $r_{\rm in}^{\rm H\,II}$ is simply $r_0 = 0$, while the initial radii of particles currently at $r_{\rm out}^{\rm H\,II}$ and $r_{\rm out}^{\rm dust}$ can be denoted by $r_0^{\rm H\,II}$ and $r_0^{\rm dust}$, respectively. We emphasize that $r_0^{\rm H\,II}$ and $r_0^{\rm dust}$ are just two working quantities, which do not correspond to any physical boundaries. The value of $r_0^{\rm dust}$ can be obtained by noting that a particle currently at $r_{\rm out}^{\rm dust}$ has just been reached by the expanding shell and has not yet moved from its initial radius $r_0^{\rm dust}$, so that $r_0^{\rm dust} = r_{\rm out}^{\rm dust} = 22$ pc. The value of $r_0^{\rm H\,II}$ can be inferred from the conservation of mass. In the initial state

$$\frac{4}{3}\pi (r_0^{\rm H\,II})^3 n_0 = M_{\rm H\,II}, \tag{A.1}$$

$$\frac{4}{3}\pi \left((r_0^{\rm dust})^3 - (r_0^{\rm H\,II})^3\right) n_0 = M_{\rm dust}, \tag{A.2}$$

where $M_{\rm H\,II}$ is the mass inside the sphere with radius $r_0^{\rm H\,II}$ and $M_{\rm dust}$ is the mass inside the shell with inner and outer radii $r_0^{\rm H\,II}$ and $r_0^{\rm dust}$, respectively, as shown in the left panel of Fig. A.1. From the previous equations we can write

$$r_0^{\rm H\,II} = r_0^{\rm dust} \left(\frac{M_{\rm dust}}{M_{\rm H\,II}} + 1\right)^{-1/3}. \tag{A.3}$$

We calculate the mass of ionized gas based on the size of the nebula and on the mean electron density of 12.3 cm^{-3}, derived from the radio data (Sect. 4.2.2). Taking into account the contribution from ionized helium (Celnik 1985), we obtain $M_{\rm H\,II} = 1.2 \times 10^4\,M_\odot$. For the mass of the dust shell we use the results of Heyer et al. (2006; Sect. 2), $M_{\rm dust} = 8.6 \times 10^4\,M_\odot$. As a result, $r_0^{\rm H\,II} = 11$ pc. With the three known radii in the initial state, $(0, r_0^{\rm H\,II}, r_0^{\rm dust})$, and their corresponding values in the present state, $(r_{\rm in}^{\rm H\,II}, r_{\rm out}^{\rm H\,II}, r_{\rm out}^{\rm dust})$, we can derive an expansion law as shown in Fig. A.2. With only three data points, we consider the simplest description of the expansion by writing r as a piecewise linear function of r_0. This is in any case sufficient to describe the two clear regimes seen in Fig. A.2: the expansion of the H II region (slope larger than 1) and the compression of the ISM within the outer shell (slope smaller than 1). The expansion law is hence given by $r = \alpha r_0 + \beta$, where $\alpha = 1.09, \beta = 7$ pc for the H II region ($r_0 < r_0^{\rm H\,II}$) and $\alpha = 0.27, \beta = 16$ pc for the dust shell ($r_0^{\rm H\,II} \le r_0 \le r_0^{\rm dust}$).

Now consider a cartesian coordinate system with z-axis along the line of sight and x- and y-axes in the plane of the sky, along the trace of the Galactic plane and along the rotation axis, respectively. The initial uniform magnetic field can be written in these Cartesian coordinates as

$$\boldsymbol{B}_0 = B_{0x}\,\boldsymbol{e}_x + B_{0y}\,\boldsymbol{e}_y + B_{0z}\,\boldsymbol{e}_z, \tag{A.4}$$

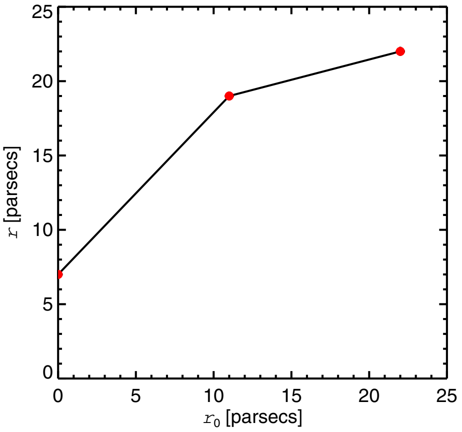

Fig. A.2. Radial expansion law derived from the three known radii in the initial, r_0, and final, r, states (red filled circles). The black curve is described by a piecewise linear function of the form $r = \alpha r_0 + \beta$, with $\alpha = 1.09$, $\beta = 7$ pc for $r_0 < r_0^{\rm H\,II}$ and $\alpha = 0.27$, $\beta = 16$ pc for $r_0^{\rm H\,II} \leq r_0 \leq r_0^{\rm dust}$.

with

$$B_{0x} = B_0 \sin\theta_0 \cos\phi_0$$
$$B_{0y} = B_0 \sin\theta_0 \sin\phi_0$$
$$B_{0z} = B_0 \cos\theta_0, \tag{A.5}$$

where θ_0 and ϕ_0 are the polar and azimuthal angles, respectively, i.e. θ_0 is the angle between $\boldsymbol{B}_0$ and the line of sight, while ϕ_0 gives the plane-of-the-sky direction of $\boldsymbol{B}_0$ with respect to the Galactic plane ($\phi_0 = 0°$ for $\boldsymbol{B}_0$ parallel to the Galactic plane).

The vector potential associated with $\boldsymbol{B}_0$ is

$$\boldsymbol{A}_0 = B_{0y} z\, \boldsymbol{e}_x + B_{0z} x\, \boldsymbol{e}_y + B_{0x} y\, \boldsymbol{e}_z, \tag{A.6}$$

which satisfies the condition $\boldsymbol{B}_0 = \nabla \times \boldsymbol{A}_0$. We use the frozen-in approximation and assume that the magnetic field evolves from the initially uniform configuration following the radial expansion of the gas. The vector potential in the final state is given by (see Eqs. (4) to (10) in Parker 1970)

$$\boldsymbol{A}(\boldsymbol{r}) = (\nabla \boldsymbol{r}_0) \cdot \boldsymbol{A}_0(\boldsymbol{r}_0), \tag{A.7}$$

and the resulting magnetic field works out to be

$$\boldsymbol{B}(\boldsymbol{r}) = \left(\frac{r_0}{r}\right)^2 B_{0r}\, \boldsymbol{e}_r + \frac{r_0}{r}\frac{{\rm d}r_0}{{\rm d}r}(B_{0\theta}\, \boldsymbol{e}_\theta + B_{0\phi}\, \boldsymbol{e}_\phi). \tag{A.8}$$

The previous equation, written in spherical coordinates, clearly shows the change in both the normal (radial) and tangential components of the magnetic field, relative to the expansion front.

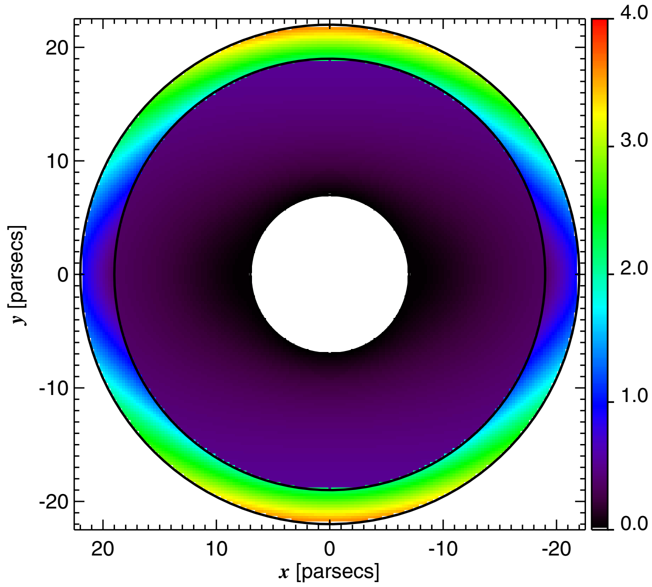

Fig. A.3. Ratio of the field strength B/B_0 for a vertical slice through the centre of the bubble-shell structure (xy plane). The initial field $\boldsymbol{B}_0$ is on the plane of the sky ($\theta_0 = 90°$) and along x ($\phi_0 = 0°$). The three black circles delineate the radii of the Rosette H II and dust shells: $r_{\rm in}^{\rm H\,II} = 7$ pc; $r_{\rm out}^{\rm H\,II} = r_{\rm in}^{\rm dust} = 19$ pc; and $r_{\rm out}^{\rm dust} = 22$ pc.

We create a 3D cartesian grid of $181^3 = 5\,929\,741$ voxels, each equivalent to 0.25 pc (0$'$.5 at the distance of the Rosette), with the bubble-shell structure located at the origin. The resolution of the model is finer than that of the observations, which is needed to have the required sampling to compute the integrals along the line of sight. We use Eq. (A.8) along with the expansion law of Fig. A.2 to calculate the magnetic field strength in every pixel of the grid. Figure A.3 shows how the field strength in the shell, B, varies relative to the initial field strength, B_0. The map corresponds to a vertical cut through the centre of the shell for an initial field with $(\theta_0, \phi_0) = (90°, 0°)$, therefore on the plane of the sky and along the Galactic plane. Figure A.3 illustrates that the largest compression of the field lines occurs towards the equator of the shell, or in the direction perpendicular to the initial field $\boldsymbol{B}_0$, where the ratio B/B_0 is seen to increase from the centre to the outer radius of the dust shell. The change in expansion law at the boundary between the H II and dust shells, $r = 19$ pc, results in a discontinuity in the tangential component of the magnetic field. On the other hand, close to the poles of the shell, or along $\boldsymbol{B}_0$, the field lines are little disturbed, with the ratio B/B_0 continuously increasing from the centre to $B/B_0 = 1$ at the boundary of the dust shell. Owing to the axial symmetry of the magnetic field model, the map of Fig. A.3 is reproduced in every plane about the direction of the initial field $\boldsymbol{B}_0$.